



How beech ecophysiology shapes temperate forest gross primary productivity – Part 1: A wavelet-based framework for extracting seasonal dynamics

Jonathan Bitton¹, Catherine Charles¹, Bernard Longdoz¹, Bernard Heinesch¹

5 ¹Biosystems Dynamics and Exchanges, TERRA Teaching and Research Center, Gembloux Agro-Bio Tech, University of Liege, Gembloux, Belgium

Correspondence to: Jonathan Bitton (Jonathan.bitton@uliege.be)

Abstract. Long-term eddy covariance (EC) records provide unique opportunities to investigate how seasonal carbon dynamics shape interannual and decadal trends in forest carbon uptake. Yet extracting reproducible phenological and structural information from noisy, non-stationary gross primary productivity (GPP) time series remains challenging. Here we present a wavelet-based analytical framework that directly exploits the time-frequency structure of GPP signals to identify repeated seasonal features. This approach departs from standard wavelet applications by analyzing the full set of wavelet coefficients as an interpretable structure to systematically detect and characterize recurrent patterns, including moderate-amplitude events that are typically overlooked by significance-based or visually driven wavelet analyses. Building on this foundation, we introduce a novel Wavelet Area Interpretation (WAI) method that extracts three complementary indicators of seasonal GPP dynamics (IRise for rising rate; IPeak for peak productivity; IDrop for mid-season decline) and derives carbon-uptake phenological markers within a unified workflow. Together, these metrics provide a coherent representation of the timing, magnitude and shape of the seasonal GPP cycle. We apply this framework to long-term EC records from three contrasting ICOS-labelled European beech-dominated forests (DE-Hai, DK-Sor, FR-Hes), demonstrating its ability to reveal both structural differences among sites and divergent long-term trajectories in carbon uptake. Benchmarking against classic smoothed GPP reference values confirms the robustness of IRise and IPeak and clarifies the inherent uncertainties associated with mid-season metrics. Ecologically, the indicators uncover consistent contrasts in seasonal structure: rapid spring rise at FR-Hes, muted mid-season decline at DK-Sor, and early cessation of uptake at DE-Hai. They reveal opposing multi-decadal trends, with peak productivity increasing in the managed stands but declining in the unmanaged old-growth forest. The negative association between IRise and mid-season drop timing further suggests intra-seasonal trade-off linking early-season vigor to mid-season susceptibility. Overall, this study provides a novel, scale-aware approach for extracting seasonal information from noisy time series and demonstrates how WAI-derived indicators can yield new insights into the mechanisms driving long-term variability across sites and applications.



1 Introduction

30 The past century has seen remarkable advancements in measurement and communication technologies, fostering the growth and maturity of various research domains (Krapivin and Shutko, 2012; Pandey and Sharma, 2021; Trankler and Kanoun, 2001). Among these, the increasing availability of long, high-frequency environmental time series has transformed ecosystem science, enabling the investigation of biological and climatic processes across a wide range of temporal scales (Allan et al., 2018; Krapivin et al., 2015; Marvin et al., 2016). At the same time, this “data-rich” context poses an analytical
35 challenge: extracting interpretable and reproducible information from signals that are inherently noisy, often non-stationary, and shaped by overlapping processes (e.g., seasonality, trends, extremes, and legacy effects) (Ascough et al., 2008; Oliveira et al., 2012; Reichman et al., 2011).

Methods designed to decompose time series into components operating at different temporal scales have therefore become central to contemporary environmental research (Platt and Denman, 1975). Spectral analysis based on the Fourier transform
40 (FT) remains foundational for characterizing the frequency content of a signal (Percival and Walden, 1993). However, the FT represents a signal in the frequency domain without explicit time localization, which makes it less suited for detecting time-localized events (e.g., abrupt changes, short-lived anomalies, or irregular seasonal disturbances) that can be ecologically meaningful (Debnath and Shah, 2015; Farge, 1992). This limitation has motivated the development and adoption of time-frequency methods in which information is jointly represented in time and in frequency (or scale). Wavelet
45 transforms (WT) provide such a representation by convolving the signal with localized analyzing functions (wavelets) across scales, thereby enabling the study of how dominant modes of variability evolve through time (Mallat, 2009).

Because many ecological and environmental time series are non-stationary and contain transient or discontinuous components, the WT has become an established tool in ecology and Earth sciences (Moreaux et al., 2020). Wavelet analysis is now used to study a broad range of processes, from population cycles (Hudson et al., 2011) to climate-ecosystem
50 couplings (Carl et al., 2013), precisely because it can isolate variability at specific time scales while preserving temporal localization. Practical guides and standardized toolkits, most notably Torrence and Compo (1998), have facilitated the diffusion of wavelet methods beyond specialist communities, including the formalization of commonly used significance testing procedures based on idealized noise backgrounds. Yet, despite this success, wavelet analyses in ecology often rely on a limited subset of coefficients or summary diagnostics, with methodological choices (wavelet family, normalization,
55 thresholding, and significance conventions) frequently inherited from precedent rather than tailored to the signal features of interest (e.g., Carl et al., 2013; Moreaux et al., 2020; Schaller et al., 2017). This can bias interpretation toward only the most prominent patterns and may obscure repeated but moderate-amplitude events that nevertheless carry strong ecological meaning.

These methodological questions are particularly relevant for ecosystem carbon-cycle studies based on eddy covariance (EC)
60 data. EC time series provide continuous observations of net ecosystem exchange (NEE) and derived flux components such as gross primary productivity (GPP), enabling mechanistic investigations of seasonal carbon dynamics and their sensitivity to



65 climate (Aubinet et al., 2012). However, extracting phenological transition dates and seasonal features from EC-derived GPP remains challenging because daily flux signals are noisy and site-specific seasonal shapes can differ substantially (Moffat et al., 2007). Recent syntheses show that different smoothing choices and phenology extraction methods (e.g., threshold versus derivative approaches) can shift inferred start and end of season dates by weeks, which in turn affects trend estimates and cross-site comparisons (Panwar et al., 2023). These uncertainties are exacerbated at sites where seasonal transitions are gradual, where growing seasons are asymmetric, or where multiple intra-seasonal perturbations occur (Xie et al., 2023).

70 In European temperate forests, these challenges intersect with a pressing ecological question: how do seasonal GPP dynamics and carbon uptake phenology shape long-term forest carbon sequestration? European beech (*Fagus sylvatica* L.) forests are central to this question because they dominate large areas of Central and Western Europe (Chiesi et al., 2016) and have shown pronounced sensitivity to drought and heat, with impacts including reduced photosynthetic activity, early senescence, and legacy effects after severe events (Campioli et al., 2011; Hesse et al., 2023; Leuschner, 2020). Meanwhile, multi-decadal EC records indicate that carbon uptake trajectories can differ markedly among beech-dominated stands, reflecting interactions among climate regime, stand age, and management (Gennaretti et al., 2020; Kulla et al., 2023; Xiao et al., 2026). Understanding such contrasts requires metrics that go beyond simple seasonal integrals, and that explicitly quantify seasonal structure, e.g., the spring rise, the peak assimilation capacity, and the extent of mid-season depression.

75 Here we propose and apply a wavelet-based framework designed to address two related limitations in current practice: (i) the tendency to focus on a restricted subset of prominent wavelet outputs and (ii) the reliance on significance testing frameworks that may discard relevant coefficients when the assumed noise background is not appropriate (Cazelles et al., 2014). Building on the mathematical structure of the WT and its time-scale localization properties, we introduce an alternative perspective that treats wavelet coefficients as a systematic basis for detecting repeated events in non-stationary signals, rather than as isolated features evaluated primarily through statistical significance maps. The method will be illustrated using 20 years of the FR-Hes GPP signal. This choice stems from the signal's shape, characterized by well-marked diurnal and annual trends (Fig. S1), and the availability of decade-long datasets through international networks such as ICOS, NEON or FLUXNET.

80 Both these characteristics tend to complicate classical WT analyses, providing an effective illustration of the benefits of our approach.

85 From this framework, we derive indicators that summarize the seasonal structure of GPP and carbon-uptake phenological metrics. Because phenological inference from EC data can be method-dependent, we explicitly benchmark these indicators and phenological dates against estimates derived directly from smoothed GPP seasonal curves. We apply this methodology to three long-term beech-dominated EC sites DE-Hai (Hainich, Germany), DK-Sor (Sorø, Denmark) and FR-Hes (Hesse, France). These forests differ in management history, age structure, and climatic setting, providing an ideal testbed to evaluate whether wavelet-derived seasonal indicators and phenological metrics capture consistent ecological contrasts and whether site differences remain stable or change through time.

Specifically, our objectives are to: (1) evaluate the consistency of the wavelet-based indicators and phenological metrics through benchmarking against smoothed-GPP reference metrics; (2) quantify long-term trends in annual carbon fluxes and in

95



seasonal-structure indicators; and (3) test for systematic differences among sites and for potential temporal changes in these differences using linear mixed-effects models that account for shared year-to-year anomalies. In doing so, we aim to provide (i) a methodological contribution: an operational, interpretable wavelet-based event detection and interpretation strategy, and (ii) an ecological contribution: new comparative insight into how seasonal GPP structure and carbon-uptake phenology differ among long-standing beech-dominated forests across Europe.

2 Methods

2.1 Theoretical background

The wavelet transform (WT) can be perceived as an extension of the Fourier transform (FT). Both can be expressed as an inner product between a function of interest $f(x)$ and analyzing functions, all of which are derived from a single mother function (Mallat, 2009). The distinction between both transforms arises from the properties of these analyzing functions, described hereafter.

- The FT employs sine and cosine waves, which can be expressed as **complex exponentials** (Fig. 1a). These functions are **periodic**, implying that their spread encompasses the entirety of the x-axis. They depend solely on a **single parameter**, the **frequency**. Consequently, we can only extract a global coefficient for each frequency, representing the influence of this frequency component on the entire function. The coefficients are necessarily complex-valued and can be associated with a phase (which part of the sine and cosine yields the information) and an amplitude (importance of the frequency component in the function). The amplitude of the Fourier coefficients is represented for each frequency (or period) in a 2-dimensional graph, known as **periodogram** (Fig. 1c).
- The WT relies on oscillating and (approximately) compact functions, aptly named “**wavelets**” (Fig. 1b). These analyzing functions are concentrated on a **finite** portion of the x-axis, referred to as the support of the wavelet, and can be translated to cover the whole x-axis. To detect oscillatory behavior in $f(x)$, the wavelets are **scaled** to match a corresponding frequency. Therefore, wavelets depend on **two parameters**: the center of the x-axis portion where the wavelet spans (**position** or **time**, for time-varying functions) and the scale of the wavelet (**frequency**). Wavelets can be real or complex, and so are the coefficients for real functions $f(x)$. The amplitude of wavelet coefficients is represented for each couple time-frequency (or time-period) in a 3-dimensional graph, called **scalogram** (Fig. 1d).

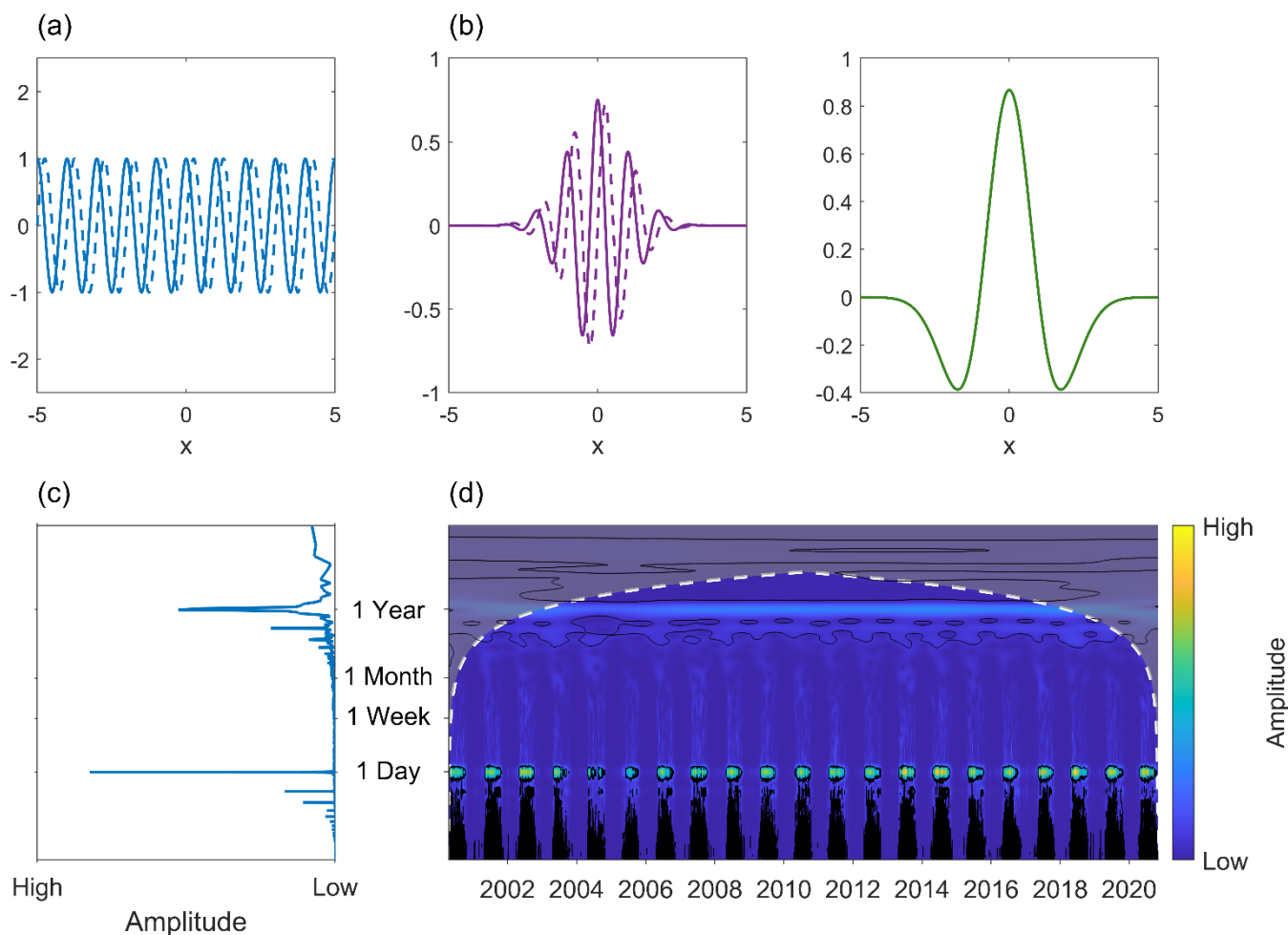


Figure 1: Graphical difference between the FT and WT. (a) Analyzing functions of the FT: sine and cosine waves, (b) Analyzing functions for the WT: Morlet wavelet (left, real and imaginary part distinguished by solid and dashed lines) and Mexican Hat wavelet (right), (c) Periodogram of the 2000–2020 FR-Hes GPP signal. The y-axis is in logarithmic scale, (d) Scalogram of the 2000–2020 FR-Hes GPP signal using the Morlet wavelet. The y-axis is in logarithmic scale. Shaded areas represent coefficients affected by edge effects, delimited by the cone of influence (Supplement S1) in white dashes. Statistically significant coefficients, assuming a red background noise, are contoured in black.

125 These descriptions provide an intuitive understanding of how both transforms extract oscillatory behaviors from a function: if $f(x)$ oscillates at a certain frequency, it will align well with the sine/cosine functions or the wavelet at the same frequency, leading to elevated coefficients. Conversely, in the absence of, or in the presence of minimal fluctuations in $f(x)$ at a specific frequency, the coefficients will approach zero, reflecting the dissimilarity between $f(x)$ and the analyzing functions. The WT, however, addresses limitations of the FT by constraining the spread of its analyzing functions, thereby enabling the study of non-stationary behaviors. Although both transforms preserve all information from $f(x)$, the FT disperses it along the infinite fluctuations of its sine/cosine waves, disabling any possibility of localization (Debnath and Shah, 2015; Farge, 135 1992).



The WT can be either continuous or discrete, with the difference lying in the permissible values for the parameters of the analyzing functions. In the continuous case, wavelets are allowed to translate across all x values, even if they overlap, and the scales of the wavelets can vary continuously, leading to redundant information on adjacent scales. The discrete transform eliminates this redundancy by restricting the set of allowable scales and translations (Abbate et al., 2002). This paper
140 concentrates solely on the continuous wavelet transform (CWT) due to its suitability for graphical representations. The scalogram in Fig. 1d results from such a continuous transform, with the Morlet wavelet as analyzing function.

An essential part of a wavelet analysis resides in the selection of the wavelet for the transform. The fundamental principle guiding this process is that the chosen wavelet should bear significant similarities with the trends sought in the signal (Farge, 1992). Several wavelets have previously found success in ecological studies. Torrence & Compo (1998) list, for complex-
145 valued functions, the Morlet and Paul wavelets and, for real ones, the Haar wavelet and a family of wavelets obtained by taking successive derivatives of the Gaussian function. By convention, these last functions are abbreviated as “DOG” followed by the order of derivation of the Gaussian function. For example, the DOG2 wavelet is the second derivative of the Gaussian function and corresponds to the opposite of the Mexican Hat wavelet. The Morlet and Mexican Hat wavelet are the most widespread wavelets used and hence have been illustrated in Fig. 1b. The other wavelets are illustrated in Fig. S2.

150 For a more comprehensive understanding of the FT and WT, one can refer to the works of Bracewell (2000), Abbate et al. (2002), and Mallat (2009).

2.2 Wavelet Area Interpretation: a novel approach for interpreting wavelet coefficients

When interpreting WT outputs, high coefficient amplitude is typically ascribed to the presence of an oscillatory behavior at
155 corresponding frequency and time in a signal. In the case of the FR-Hes dataset, the GPP scalogram displays high coefficients around a 1-year period (Fig. 1d). This reflects the annual periodicity of the forest's photosynthetic behavior due to climatic (annual course of the sun) and physiological (seasonality of leaves) factors. The daily period band exhibits even higher coefficients concentrated each year during the forest's growing season (GS), mirroring the response of chlorophyll elements to the daily course of incoming photosynthetic radiation when leaves are present. While this approach leads to
160 straightforward interpretations for pronounced trends, it proves impractical for intermediate scales, ranging between a day and a year. Coefficients in these scales occur within narrow time ranges, which can obscure the distinction of underlying phenomena and potentially cause confusion between them. Normalizing the scalogram (see Fig. S3) highlights recurring elevated coefficients in these ranges each year, although they do not always appear significant.

To fully leverage these less-pronounced but information-dense regions of the scalogram, we propose a novel interpretation
165 of wavelet coefficients, based on a mathematical perspective. This approach relies on the definition of the CWT. Considering a time-varying signal $x(t)$ and a wavelet $\psi(t)$, the CWT is expressed as:

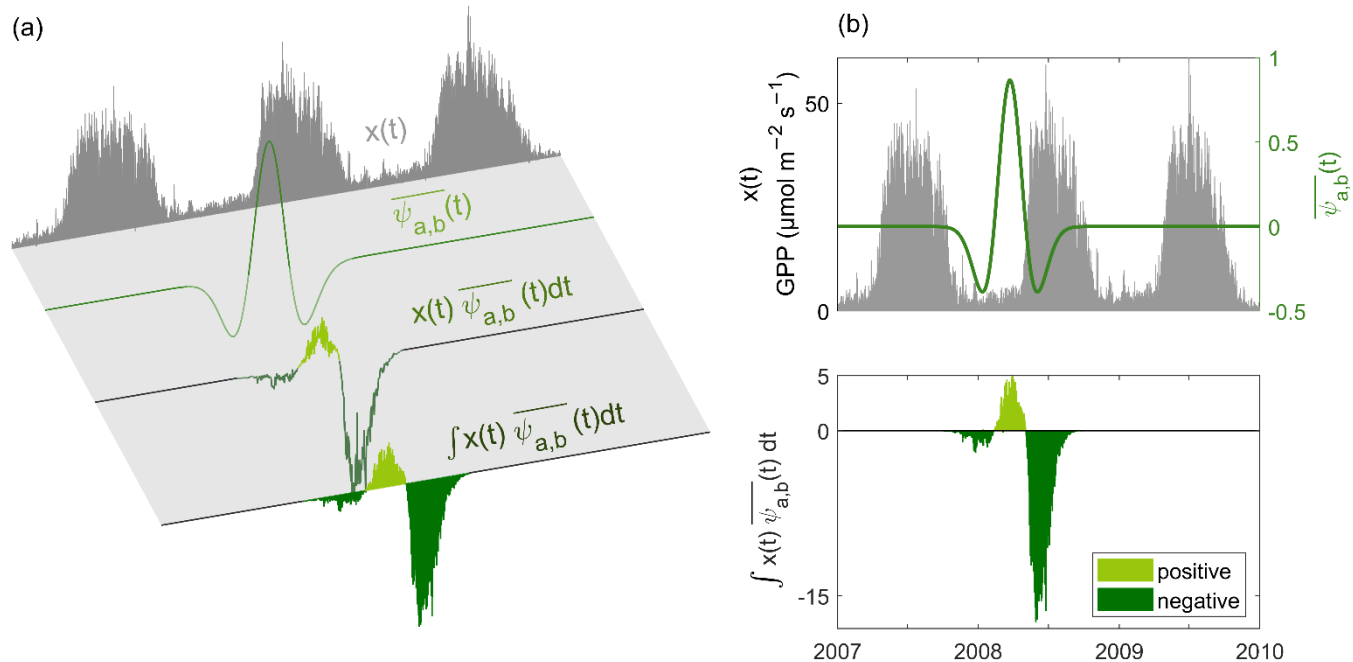


$$W(a, b) = \int_{-\infty}^{+\infty} x(t) \overline{\psi_{a,b}(t)} dt$$

Where $\bar{}$ denotes the complex conjugate and $\psi_{a,b}(t)$ is the wavelet taken at a certain scale a and time b , normalized by introducing a multiplying factor. Since our approach only requires qualitative results, this factor is omitted from further developments. According to the CWT formula, a wavelet coefficient $W(a, b)$ may be constructed by following three steps:

1. Computing the chosen wavelet at scale a and position b , i.e. $\psi_{a,b}(t) = \psi\left(\frac{t-b}{a}\right)$
2. Defining a product curve by multiplying $x(t)$ with (the complex conjugate of) the wavelet.
3. Computing the area under the product curve by positively accounting for contributions that lie above the $t=0$ axis and negatively for those below.

Figure 2 demonstrates these steps for the Mexican Hat wavelet placed at the start of April with a scale corresponding to a period of 6 months (see Fig. S4 for an example using a complex wavelet). The primary advantage of this graphical approach, named the Wavelet Area Interpretation (WAI), lies in the ability to assign an interpretation to a wavelet coefficient based on the areas contributing to its calculation. For instance, the value of the coefficient computed in Fig. 2 is governed by the third (negative) lobe of the wavelet. Graphically, the projection of the function on this lobe expresses the rising GPP values during the first peak of photosynthetic activity from May to July.



185 **Figure 2: (a) Detailed computation of a wavelet coefficient following the mathematical definition of the CWT. (b) Condensed view of the computation process. The top graph displays the Mexican Hat wavelet at a chosen scale (corresponding to a 6-month period) and time (start of April) with the GPP signal in the background (restricted to positive values for readability). The graph below illustrates the area under the product curve of the wavelet and the signal. The algebraic sum of the three contributing areas, each linked to a lobe of the wavelet, corresponds to the wavelet coefficient yielded by the WT at the selected scale and time, after normalization.**



190 WAI allows for the interpretation of individual wavelet coefficients, but selecting which coefficients to analyze among the
plethora generated by the WT is non-trivial and depends on the signal structure. Furthermore, because the contributing areas
of a coefficient are determined by the wavelet shape, the interpretability of coefficients varies among wavelets. These
considerations highlight the need to integrate WAI into a reproducible, systematic procedure. To this end, we introduce a 3-
step method (Fig. 3) for identifying and interpreting meaningful coefficients.

- 195 1. **Selecting coefficients.** Relevant coefficients are identified by representing average period bands as a function of
time. For a given period, the mean amplitude of coefficients within a narrow scale range is computed, and local
maxima in this period-band signal indicate time windows where prominent patterns occur. These maxima then
serve as the primary candidates for WAI interpretation. Wavelet choices for computing period bands are discussed
in Supplement S2.
- 200 2. **Interpreting coefficients.** After selecting relevant coefficients from identified peaks, WAI is used to interpret them
based on the most prominent contributing areas (see the procedure detailed in Fig. 2).
- 205 3. **Refining interpretations.** To reduce uncertainties into interpretations given to wavelet coefficients, the third step
involves adjusting the WT to align coefficient values with interpretations. A wide variety of possibilities exist,
among which four are detailed in Supplement S3. The final coefficient value obtained post-adjustments serves as an
indicator of the importance of a feature's presence in the signal. Consequently, we simply refer to these values as
"indicators".

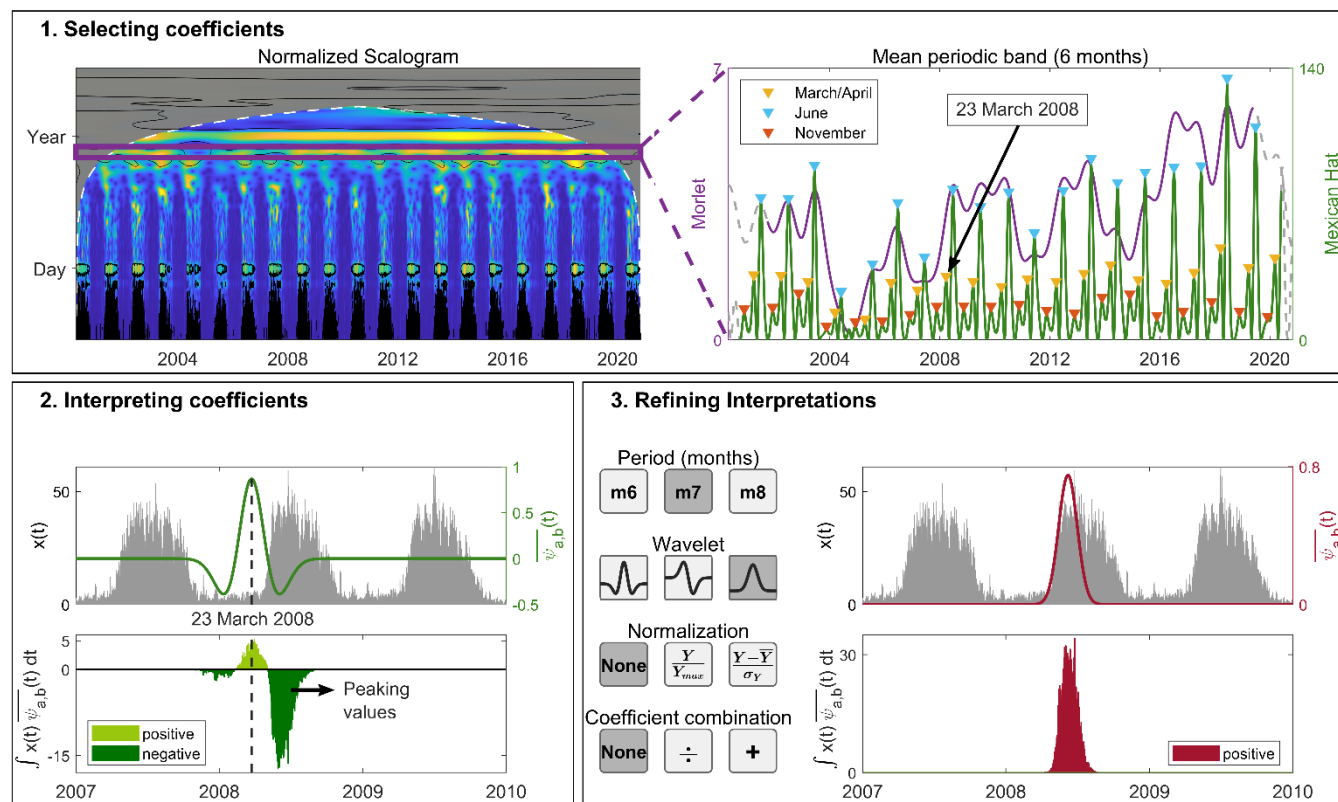


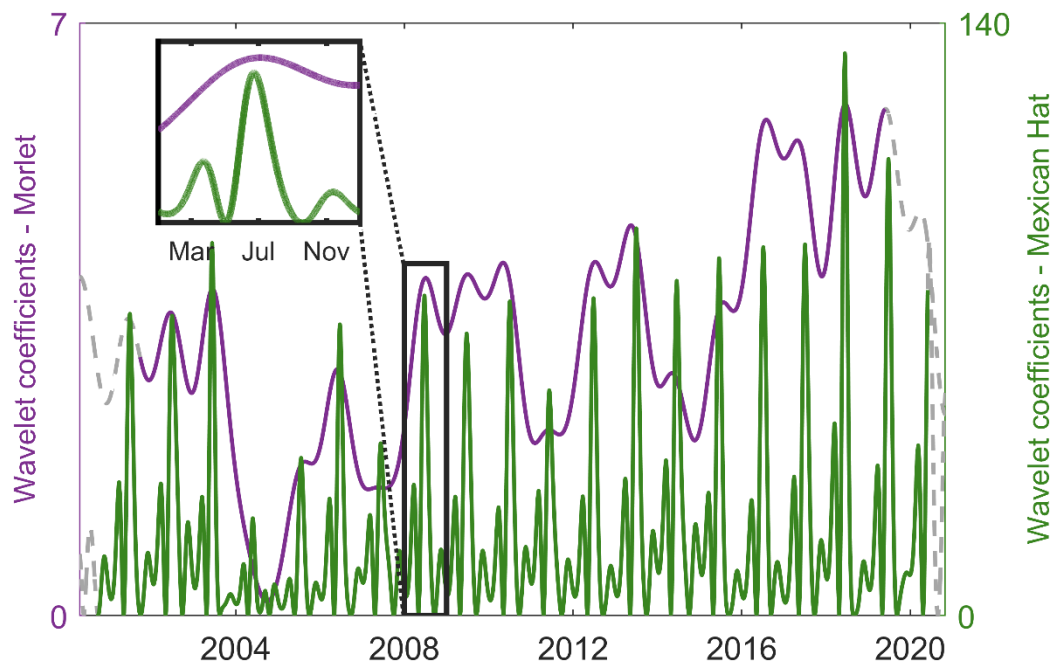
Figure 3: Schematic view of the 3-step methodology.

These guidelines are designed to seamlessly blend the newly introduced WAI approach with classical wavelet analyses by building on familiar WT outputs. They can further be adapted to specific datasets, which is done hereafter for temperate deciduous forest GPP using the FR-Hes site as a study case. Ready-to-use Python and Matlab codes are available online and all figures were produced using Matlab R2022a (The MathWorks Inc, 2022).

2.3 Application to temperate deciduous forest GPP

2.3.1 Selecting coefficients

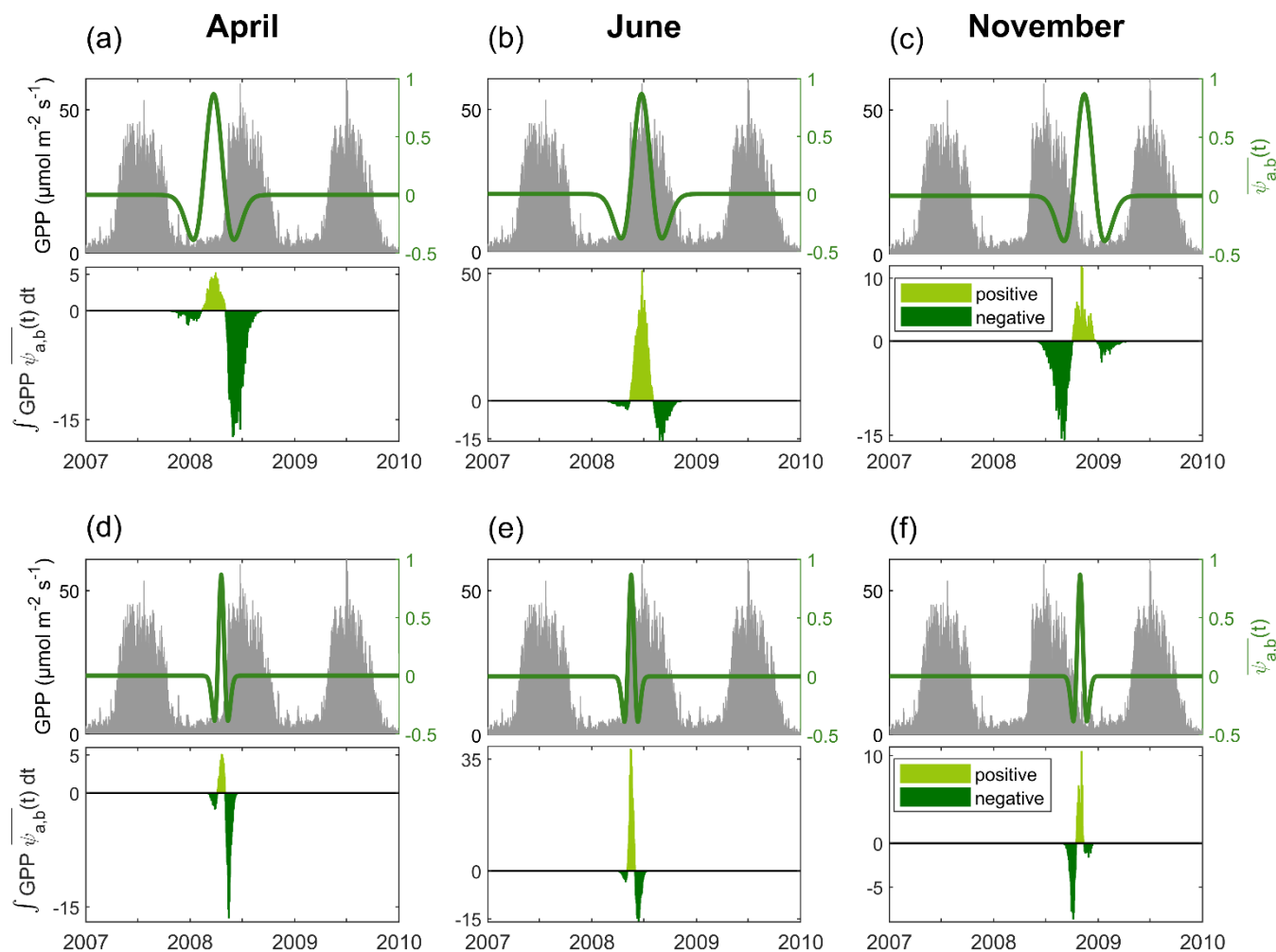
Figure 4 demonstrates the 6-month \pm 15 days band for the Morlet and Mexican Hat wavelets. Both curves exhibit multiple peaks, offering a variety of relevant choices for further investigation. A closer examination of the Mexican Hat curve can further refine this selection: the 6-month band displays three recurring peaks for each year, in April, June and November (Fig. 4, Zoom).



220 **Figure 4: Amplitude of the wavelet coefficients using the Morlet wavelet (purple) and the Mexican Hat wavelet (green) at the 6-month period band. Grey dashed curves represent coefficients affected by edge effects. Corresponding graph for the 2-month period band is given in Fig. S5.**

225 All three peaks are positioned at key periods of the GPP curve: the onset of rising values in April (second zero of the wavelet, Fig. 5a), the GPP peak in June (maximum of the wavelet, Fig. 5b) and the end of decreasing values in November (first zero of the wavelet, Fig. 5c). This repeated behavior hints to the ability of these peaks to extract specific features pertaining to the annual pattern of the GPP curve for temperate deciduous forests.

The GPP scalogram displays significant coefficients for a range of periods, from 6 months to 1–2 months (Fig. 1d). Building on the wavelet positioning for the annually recurring 6-month peaks, the corresponding 2-month peaks were identified using the WAI (Figs. 5d-f), resulting in 6 selected peaks per year.



230 **Figure 5: Computation steps for wavelet coefficients, (a-c) at a 6-month period for the three annual peaks observed with the Mexican Hat wavelet (see Fig. 4, zoom), and (d-f) at a 2-month period for their low-period counterpart.**

2.3.2 Interpreting coefficients

Based on areas that contribute most significantly to coefficient values, contrasting interpretations can be attributed to these three pairs of peaks. They are summarized in Table 1.

235 At a 6-month period, the April peak value is primarily influenced by the right lobe of the wavelet. The wavelet serves as a weighting factor, yielding high coefficients if the GPP signal reaches high values during the first half of the GS. The 2-month period focuses on the rising phase of the GPP at the onset of the GS. It will thus depend on the rate at which the forest's photosynthetic activity reaches its maximum values. The central lobe acts as an inverse weighting factor in case of a progressive GPP increase.

240 The June peak value is derived from the central part of the wavelet. At a 6-month period, its value increases if the initial GPP peak reaches high values and maintains global smoothness, with minimal to no significant summer drops. Ideally, GPP



follows a bell-shaped curve during the first half of the GS (Fig. S1) when environmental stresses are scarce. The intensity of this peak is directly related to limiting factors on leaf cover density, such as biotic stresses, winter thinning or lacking nitrates or starch reserves. The 2-month period is of less interest. It can be associated with the presence of high amplitude fluctuations in the initial GPP peak, as can result from storms or weather fronts.

The November peaks are symmetrical to the April ones, with the left lobe of the wavelet extracting the feature. Consequently, the 6-month peak represents the GPP values during the second half of the GS, marked by reduced photosynthetic activity due to dwindling incoming photosynthetic radiation. Environmental stresses, predominantly aerial or edaphic drought, can drastically accentuate this drop starting mid-July. The 2-month peak translates the rate of the GPP decline due to senescence. Similar to the April peak, the center lobe can negatively impact the 2-month coefficient if the decrease in GPP is gradual.

Table 1: Lobe of the Mexican Hat wavelet extracting information and associated interpretations for high-period (6 months) and low-period (2 months) peaks in wavelet coefficients.

	<i>April</i>	<i>June</i>	<i>November</i>
<i>Wavelet lobe</i>	Right	Center	Left
<i>6-month peak</i>	GPP values during the first half of the GS	GPP peak values and smoothness at the middle of the GS	GPP values during the second half of the GS
<i>2-month peak</i>	Rate of the GPP rise at the onset of the GS	Importance of fluctuations in the GPP peak	Rate of GPP decrease at the end of the GS

2.3.3 Indicators

Using the interpretations summarized in Table 1, we defined three indicators describing key seasonal features of the GPP cycle. Their construction relies on targeted use of wavelet coefficients at specific scales, selected to match the temporal processes they represent. Additional examples of possible indicators are provided in Supplement S4.

1. IRise: Spring rising rate

IRise quantifies *the rate at which GPP increases from the start of the GS to its seasonal maximum*. The low-period April peak identified in Table 1 reflects this early-season rise, but the Mexican Hat wavelet introduces unwanted contributions from its left and central lobes (Fig. 5d). To avoid these effects, we use the DOG1 wavelet, which consists of two symmetric lobes. The left lobe acts as a negative weight during the early increase, and the right lobe isolates upper GPP values during the first half of the season (Fig. 6a). Prior to transformation, GPP is normalized by its annual amplitude to remove sensitivity to interannual changes in absolute GPP levels.

The DOG1 scale is chosen to match the approximate 2-month duration required for GPP to reach its peak under favorable conditions. Considering an average 12-day offset between the wavelet positioning and the start of the GS (evaluated using phenological data), the right lobe should instead span approx. 48 days. Since one lobe of the DOG1 wavelet covers half of its analyzing period, a period close to 3 months reproduces this duration.



Final choice: IRise is defined as the amplitude of the April DOG1 coefficient computed at a 3-month period on a normalized
270 GPP signal.

2. IPeak: Peak productivity

IPeak represents *maximum seasonal productivity and ideally reflects the Gaussian-shaped peak of GPP*. The high-period
April peak in Table 1 captures this behavior. The Mexican Hat wavelet again includes undesired contributions from its left
and central lobes (Fig. 5a), while the DOG1 wavelet only restricts these to the left lobe. We therefore replace the DOG1
275 wavelet with a Gaussian function centered on the position of its second lobe, retaining only the contribution associated with
the seasonal maximum (Fig. 6b).

The period is selected to approximate the temporal width of the seasonal GPP peak. Contrary to the sinusoid-shaped DOG1
wavelet, the period of analysis is ill-suited to describe the extent of the Gaussian function. Using a support criterion, defined
as the portion of the axis containing 99 % of area, a Gaussian at a 7-month period (support of 121 days) closely matches the
280 expected 4-month extent of the seasonal maximum. Similar periods yield highly correlated values ($r = 0.99$ for 6 and
8 months, p -values < 0.001), ensuring robustness.

Final choice: IPeak is defined as the value of the Gaussian-based coefficient centered on the April peak using a 7-month
period on the raw GPP signal.

3. IDrop: Mid-season decline amplitude

IDrop measures *the relative difference between GPP in the first and second half of the GS*. The high-period June peak
associated with the Mexican Hat wavelet naturally captures this contrast: its central lobe reflects pre-drop GPP levels, and its
right lobe reflects post-drop levels (Fig. 5b). The coefficient amplitude therefore represents the difference in productivity
across the mid-season decline. To standardize IDrop and avoid dependence on absolute magnitudes, the June coefficient is
divided by the high-period November coefficient (Fig. 5c), yielding a ratio between early- and late-season levels that is
290 comparable across years.

The DOG1 wavelet can also represent this drop; however, high-period June peaks only emerge clearly when the decline is
pronounced. For consistency across years and sites, the systematic April and November peaks can be used as ratio
components (Fig. S6). Both approaches produce similar results ($r = 0.96$, $p < 0.001$).

Final choice: IDrop is defined as the ratio of the 6-month Mexican Hat coefficient at the June peak to the coefficient at the
295 November peak.

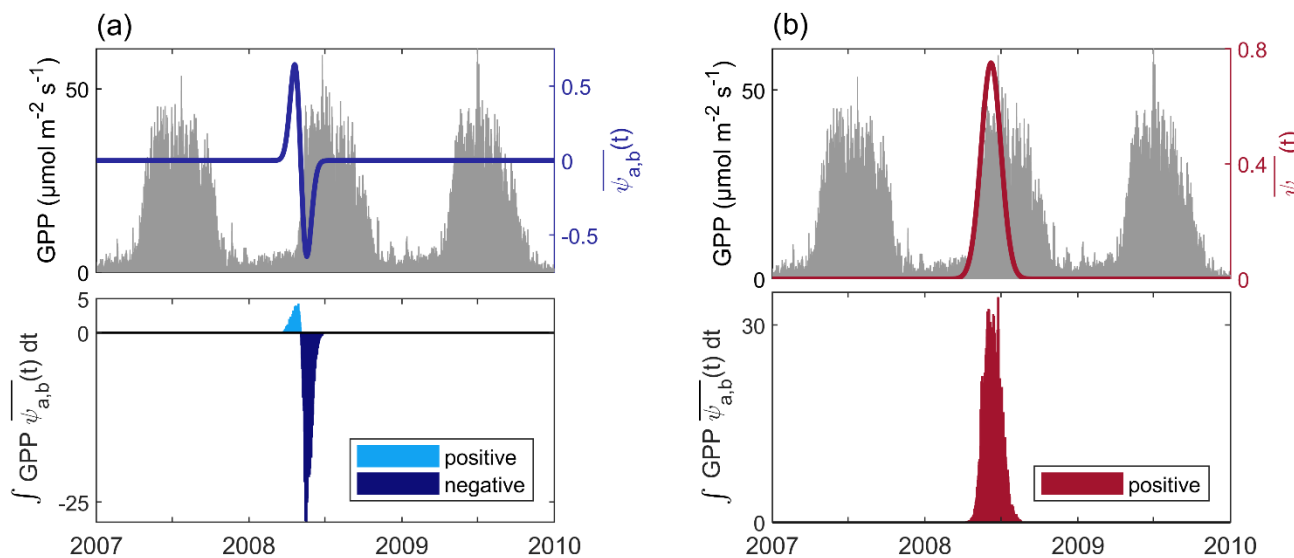


Figure 6: Computation steps for deriving (a) IRise (DOG1 wavelet) and (b) IPeak (Gaussian function). Corresponding plots for IDrop can be found in Fig. 5b and Fig. 5c.

2.3.4 Date selection

300 Peaks in period bands may correspond to discontinuity points, such as the start (Fig. 5d) or end (Fig. 5f) of a trend. Extracting the date associated with these peaks allows the automatic identification of key phenological events. Because timing precision increases at lower periods, short-period coefficients (from roughly two months down to one week, depending on noise level) are appropriate for detecting seasonal transitions. Leveraging this property, we define three phenological metrics:

305 Start of carbon uptake (CUS): In temperate deciduous forests, budburst produces a sharp increase in GPP, making the onset of carbon uptake clearly identifiable. CUS is defined as the first significant (greater than average) 2-week DOG1 peak occurring in April–May. The DOG1 wavelet is well suited to this task because its two opposite-sign lobes highlight abrupt upward changes in the signal (Fig. 6a).

310 End of carbon uptake (CUE): The decline in GPP at the end of the GS is more gradual, so a longer period is required. CUE is derived from the 2-month DOG2 coefficient, chosen for its reduced number of spurious peaks late in the year. The DOG2 wavelet is centered approx. 14 days after the inflection point of the final GPP decrease, effectively aligning the estimated date with the end of carbon uptake.

Mid-season drop (MSD): Transitions between distinct curve behaviors can also be detected using peaks in period bands, as is the case for the mid-season GPP drop timing. MSD is estimated by locating the second zero of the Mexican Hat wavelet relative to the high-period June peak (Fig. 5b), used to construct IDrop. Practically, we translate the date of the 6-month Mexican Hat June peak to the position of its next zero to obtain the MSD timing.



2.4 Data analysis

2.4.1 Study sites

320 Alongside the Hesse site (FR-Hes), two other long-standing temperate deciduous forest sites were used, from Hainich, Germany (DE-Hai) and Sorø, Denmark (DK-Sor).

FR-Hes is a temperate broadleaf deciduous forest in northeastern France. The stand originates from natural regeneration following the clear-cutting of a mature beech forest in 1965 and has been managed through regular thinnings every 5–6 years, progressively reducing the proportion of beech. European beech remains the dominant species, accompanied mainly
325 by hornbeam (*Carpinus betulus* L.) and various oak species (*Quercus* spp.). Peak leaf area index (LAI) reaches 7–8 m² m⁻² and understory vegetation is sparse due to the high canopy closure. The climate is semi-continental temperate, with a mean annual temperature of 10 °C and mean precipitation of 889 mm. The terrain is gently sloping (< 5 %) and soils are intermediate between a luvisol and a stagnic luvisol, favoring the formation of a perched water table during wet winters. An eddy-covariance tower has been operating in a central part of the forest since 1996 (Campioli et al., 2011; Granier et al.,
330 2008).

DE-Hai is located in the core zone of Hainich National Park in central Germany. It is an unmanaged, old-growth mixed deciduous forest characterized by a highly heterogeneous structure and a wide age distribution ranging from young regeneration to trees older than 250 years. European beech dominates the canopy (60–70 % of biomass), with ash (*Fraxinus excelsior* L.) and sycamore maple (*Acer pseudoplatanus* L.) as co-dominant species, alongside scattered hornbeam, elm and
335 other deciduous species. The stand contains a notably high amount of deadwood (approx. 10 % of above-ground biomass) and maximum leaf area index (LAI) reaches about 5 m² m⁻². The climate is humid continental, with a mean annual temperature of 8.3 °C and mean precipitation of 744 mm. The landscape is gently sloping (< 5 %) and soils are predominantly cambisols. The forest extends continuously for several kilometres around the eddy-covariance tower, which was installed in 1999 (Mund et al., 2020; Tamrakar et al., 2018).

340 DK-Sor is a managed beech forest located in Lille Bøgeskov on the island of Zealand, Denmark. The dominant stand surrounding the flux tower was planted in 1921 and is regularly thinned (about 20 % every 10 years). The forest is primarily composed of European beech, with approx. 20 % of the area occupied by dispersed patches of conifers, mainly Norway Spruce (*Picea abies* (L.) H. Karst.) and larch (*Larix decidua* Mill.). Tree height increased from 24 m in 1996 to 28 m in 2018, and peak LAI is typically 4–5 m² m⁻². The site has a temperate maritime climate, with a long-term mean annual
345 temperature of 9 °C and mean precipitation of 640 mm. The terrain is flat, and the soils are brown earths (Alfisol/Mollisol) with a 10–40 cm organic layer and acidic upper horizons. The flux tower, operating since 1996, is located centrally within a 1–2 km wide forest block (Dellwik and Jensen, 2005; Pilegaard and Ibrom, 2020).



2.4.2 Data computation

Carbon concentration and flux data were compiled for the three long-term eddy-covariance sites. For DK-Sor, we used the
350 Warm Winter dataset covering 1996–2020 (Ibrom et al., 2022). For DE-Hai, data were obtained from FLUXNET products
for the period 2000–2023 (Knohl et al., 2025). Finally, for FR-Hes, we combined PI-processed data from 1997 to 2014 with
the Warm Winter records for 2014–2020 (Cuntz et al., 2021). For the PI-processed period, GPP was derived using the
nighttime partitioning algorithm implemented in the standard REdDyProc routine (Wutzler et al., 2018). More details on the
constitution of the FR-Hes dataset are given in the companion paper that forms the second part of this study. LAI estimates
355 were available before 2013 at FR-Hes.

Based on GPP time series, we derived three seasonal indicators (IRise, IPeak and IDrop) together with phenological metrics
(CUS, MSD, CUE) using the previously described WAI-based approach. Due to increased small peaks surrounding the CUS
at DK-Sor, a filter on coefficient signs (i.e., sign must be negative to denote the growing part of the peak) was applied to
reduce estimation bias.

360 We additionally defined the carbon uptake length (CUL) as CUE-CUS. These metrics were derived for each year available at
the three forest sites.

2.4.3 Benchmarking

To validate the WAI-derived estimates, we computed reference values for the three indicators and phenological markers
directly from the GPP curves.

365 Daily GPP was first smoothed using a 2-week sliding median. Seasonal amplitude was approximated as the interquartile
range of the smoothed GPP curve, defined as the difference between the 95th and 5th percentile of the yearly GPP data. This
amplitude served as a relative reference for all threshold-based definitions. Reference phenological markers were then
extracted as follows:

- CUS: first day when smoothed GPP exceeds 30 % of the seasonal amplitude for at least 7 consecutive days. The
370 end of the rapid growth phase is identified when GPP exceeds 70 % of the amplitude.
- CUE: first day after the peak when smoothed GPP falls below 20 % of the seasonal amplitude for at least 7
consecutive days. To increase temporal precision, a 1-week smoothing window was applied for this marker.
- MSD: first day after the peak when smoothed GPP drops below 90 % of the seasonal amplitude for at least 7
consecutive days.

375 Based on these dates, the following reference indicators were derived:

- IRise: slope of a 30-day smoothed and amplitude-normalized GPP curve, calculated between the start and end of the
rapid growth phase (as defined in the CUS procedure).
- IPeak: mean GPP value during the peak period, defined as the interval between the end of rapid growth and the
MSD.



380 - IDrop: ratio of mean GPP before the MSD (CUS to MSD) to mean GPP after the MSD (MSD to CUE).

WAI-derived indicators and phenological markers were compared to their GPP-based reference counterparts using linear regressions. This benchmarking analysis evaluates the ability of the WAI-approach to capture seasonal GPP dynamics and reproduce key phenological transitions in carbon uptake.

2.4.4 Evaluating annual trends

385 For all three sites, mean annual CO₂ concentration, annual sums of carbon fluxes (NEE, GPP, Reco), indicator values (IRise, IPeak, IDrop) and phenological markers (CUS, MSD, CUE) were computed. Annual trends were identified using linear regressions and confidence intervals for estimated parameters were computed using student distributions with 95 % confidence.

To test whether the indicators and phenological markers differed among sites and whether site differences changed over
390 time, we used linear mixed-effects models. For each indicator, we fitted a model including Site (three levels: FR-Hes, DE-Hai, DK-Sor), YearC (centered years), and their interaction as fixed effects, and an intercept varying by Year as a random effect. This formulation accounts for the fact that measurements from the same calendar year share unmeasured environmental conditions (e.g., climate anomalies), while also allowing each site to exhibit its own temporal trend.

The model for each indicator took the form:

$$395 \quad Y_{i,t} = \beta_{0,\text{Site}(i)} + \beta_{1,\text{Site}(i)} \cdot \text{YearC}_t + u_t + \varepsilon_{i,t}$$

Where $u_t \sim N(0, \sigma_{\text{Year}}^2)$, captures random year-to-year variation and $\varepsilon_{i,t} \sim N(0, \sigma^2)$ captures residual variation.

Models were fitted using restricted maximum likelihood, and the significance of fixed effects was evaluated using Satterthwaite's approximation of denominator degrees of freedom.

To compare sites, we used estimated marginal means (EMM) at the mean Year (i.e., YearC = 0), which provide site means
400 adjusted for the model's covariates and unequal coverage of years among sites. Pairwise contrasts between sites (FR-Hes vs DE-Hai, FR-Hes vs DK-Sor, DE-Hai vs DK-Sor) were performed on these EMMs using Wald tests based on the fixed-effects coefficient covariance matrix.

In addition, we tested the Site×Year interaction to determine whether differences between sites remained constant through
405 time or evolved (i.e., differences in temporal slopes). When the interaction was significant, we interpreted site contrasts as differences at the reference Year (YearC = 0) and described how site differences changed over time based on the fitted slopes.



3 Results

3.1 Annual carbon fluxes

On average, all three sites act as carbon sinks, with DE-Hai showing the largest net uptake ($-501 \text{ gC m}^{-2} \text{ yr}^{-1}$), followed by
 410 FR-Hes ($-410 \text{ gC m}^{-2} \text{ yr}^{-1}$), whereas DK-Sor exhibits a much lower of $-208 \text{ gC m}^{-2} \text{ yr}^{-1}$. However, DK-Sor carbon sinking
 capacity increases approx. two times faster than FR-Hes (Table 2). In contrast to both sites, annual NEE at DE-Hai is
 increasing, which implies more CO₂ emission proportionally to absorption over years. All three sites exhibit strongly
 significant annual GPP trends, in accordance with NEE dynamics (i.e., increase for FR-Hes and DK-Sor, decrease for DE-
 Hai). Although variations in Reco follow the same pattern, these are less pronounced and less significant (37 %, 40 % and
 415 63 % less important respectively for FR-Hes, DE-Hai and DK-Sor). NEE dynamics are therefore governed by variations in
 GPP rather than Reco.

Table 2: Mean annual values and long-term trends (slope \pm 95 % CI) of NEE, GPP, and Reco for the three study sites. Slope estimates are derived from linear regressions over the full period available for each site; p-values indicate the significance of temporal trends.

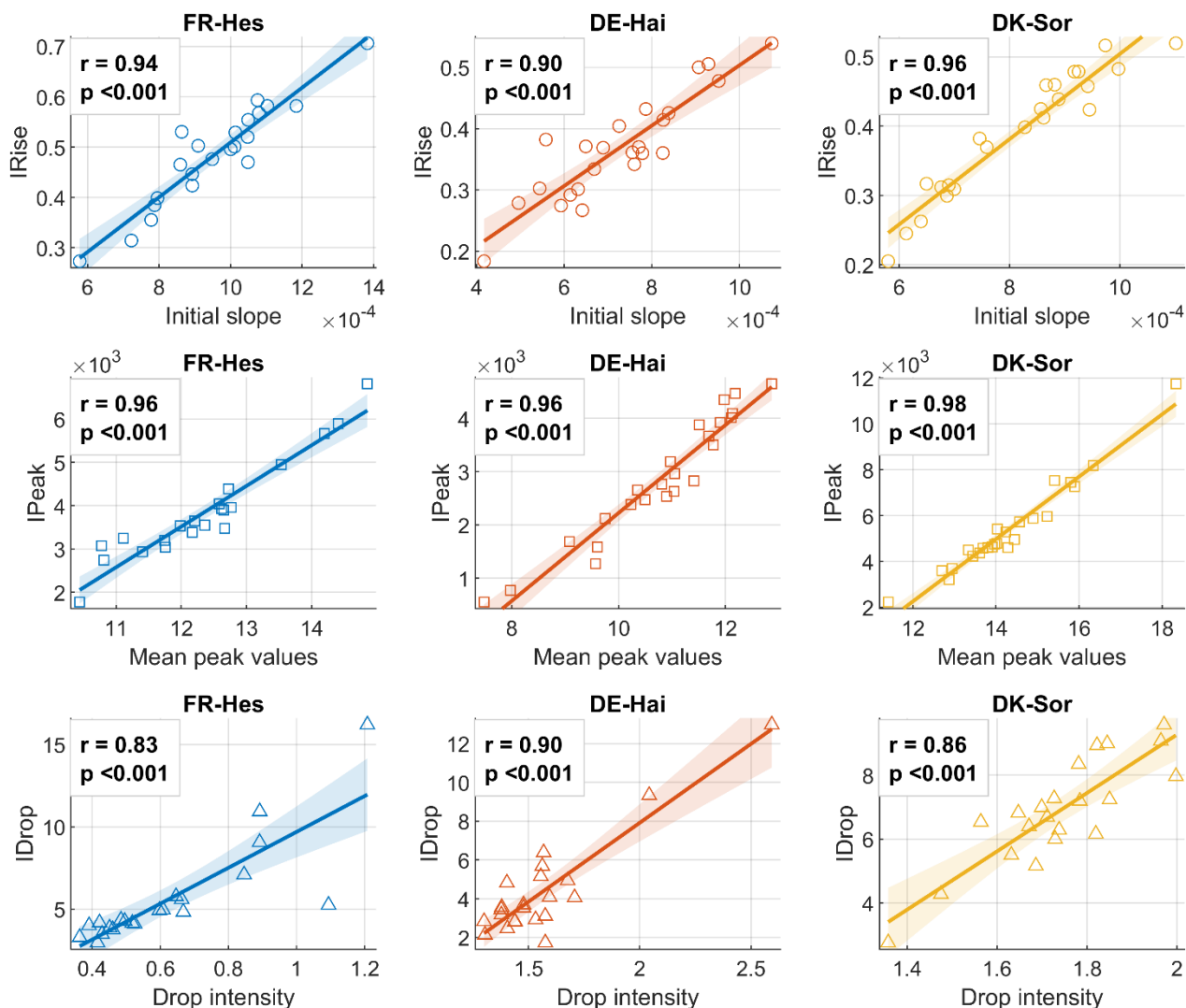
	NEE ($\text{gC m}^{-2} \text{ yr}^{-1}$)			GPP ($\text{gC m}^{-2} \text{ yr}^{-1}$)			Reco ($\text{gC m}^{-2} \text{ yr}^{-1}$)		
	Mean	Slope	p-value	Mean	Slope	p-value	Mean	Slope	p-value
FR-Hes	-410	-5.6 ± 9.4	0.23	1814	15.6 ± 9.2	0.002	1406	9.89 ± 9.1	0.035
DE-Hai	-501	6.8 ± 5.2	0.012	1559	-17.0 ± 8.7	<0.001	1058	-10.2 ± 7.4	0.009
DK-Sor	-208	-15.7 ± 5.1	<0.001	2053	24.8 ± 9.5	<0.001	1845	9.2 ± 9.5	0.058

420 CO₂ concentrations have significantly increased at all sites (slopes of 0.026 ± 0.0092 , 0.055 ± 0.0097 and
 $0.075 \pm 0.012 \text{ ppm yr}^{-1}$ respectively for FR-Hes, DE-Hai and DK-Sor, all p-values < 0.001). In addition, LAI and CO₂
 concentrations were significantly correlated ($r = 0.78$, $p = 0.0016$) at FR-Hes, when thinning years were excluded.

3.2 Benchmarking

Comparison between indicators and reference values (Fig. 7) indicates global accordance, all correlations being highly
 425 significant ($p < 0.001$). In general, IPeak shows the strongest accordance between methods ($r = 0.96\text{--}0.98$), with IRise
 following suit ($r = 0.90\text{--}0.96$). IDrop comparisons presents more scatter ($r = 0.83\text{--}0.90$), with large drops dominating the
 relationships. Years with relatively early drops and strong late GPP drops tend to be more severely punished using the WAI
 and contribute strongly to the scatter. A significant example is year 2016 at FR-Hes, which once excluded yields a much
 higher correlation ($r = 0.95$).

430



435

Figure 7: Benchmarking of the three GPP Indicators: initial slope (IRise, top), peaking values (IPeak, middle) and mid-season drop intensity (IDrop, bottom). WAI-derived indicators (y-axis) are compared to corresponding values estimated using GPP time series (x-axis) for three forest sites (FR-Hes, DE-Hai and DK-Sor). Computation details are given in the Sect. 2.4.3. Correlations and p-values are given for each relationship.

440

As for indicators, all phenological markers were significantly correlated to reference dates ($p < 0.001$ for all correlations, see Fig. S7). When fixing the intercept to 0, slopes are all in range 0.99–1 for CUS and 1.04–1.06 for CUE. Estimated MSD on smoothed GPP is less correlated with WAI-derived metrics ($r = 0.69$ – 0.80): slopes are highly different from 1 (in range 0.36–0.63) and significant shifts were found between metrics and reference dates (up to 40 days). Relationships at DK-Sor present the lowest correlation with reference values for all metrics. At this site, early GPP increases and late GPP decreases were more progressive, which lead to more uncertainty on CUS and CUE.



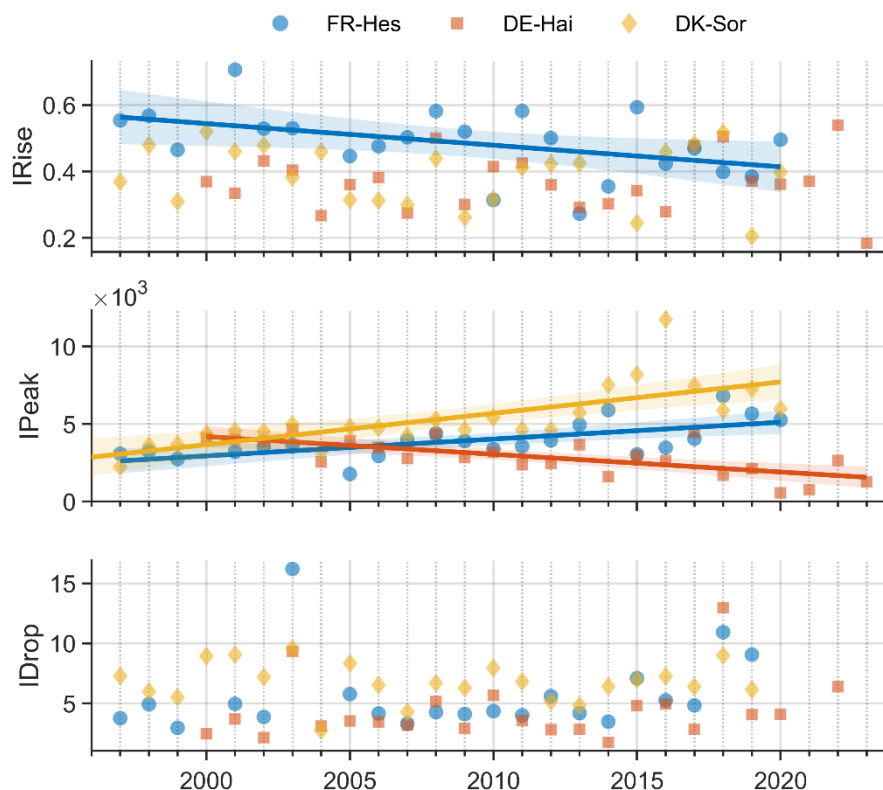
3.3 Environmental drivers of IRise

The mixed-effects models revealed substantial differences among sites for several indicators (Table 3).

445 **Table 3: Estimated marginal means (EMM) evaluated at a reference year (center point of each dataset) from linear mixed-effects model with Site, centered Year and Site×Year as fixed effects and a random intercept for Year. Grouping letters (referring to FR-Hes, DE-Hai and DK-Sor in order) denote homogenous groups from Holm-adjusted pairwise contrasts. Sites sharing a letter are not significantly different at $\alpha=0.05$. P-values are given for significant differences between sites and for Site×Year interactions. See Fig. 8 and Fig. 9 for time-varying differences. If Site×Year is significant, EMM and letters apply at reference year. Model results are detailed for each indicator (IRise, IPeak, IDrop) and phenological marker (CUS, MSD, CUE, CUL).**

	EMM (FR-Hes)	EMM (DE-Hai)	EMM (DK-Sor)	Grouping	p(Site)	p(Site×Year)
IRise	0.48 ± 0.038	0.37 ± 0.038	0.39 ± 0.038	a b b	< 0.001	0.104
IPeak	3995 ± 459	3076 ± 452	5630 ± 444	a b c	< 0.001	< 0.001
IDrop	5.55 ± 1.04	4.10 ± 1.03	6.72 ± 1.01	a b c	< 0.001	0.151
CUS	117.9 ± 3.4	120.3 ± 3.4	119.5 ± 3.4	a a a	0.380	0.451
MSD	214.4 ± 4.8	226.3 ± 4.7	210.7 ± 4.6	a b a	< 0.001	0.822
CUE	309.3 ± 3.1	298.3 ± 3.1	303.6 ± 3.0	a b c	< 0.001	0.860
CUL	190.9 ± 4.9	180.0 ± 4.8	184.4 ± 4.7	a b c	< 0.001	0.885

450 No significant Site×Year interaction was observed for IRise ($p = 0.104$), indicating that differences among sites remain approximately constant through time. EMMs indicated that IRise values were on average higher at FR-Hes (0.48 ± 0.038) than at DK-Sor (0.39 ± 0.038) and DE-Hai (0.37 ± 0.038). Pairwise contrasts confirmed this, as FR-Hes presented significantly higher IRise than DE-Hai (difference: $\Delta = 0.12$, $p < 0.001$) and DK-Sor ($\Delta = 0.1$, $p < 0.001$). IRise values between the two latter sites were not significantly different. Only FR-Hes shows a significant trend over time (slope =
455 -0.0065 , $p = 0.032$), IRise values decreasing over years (Fig. 8).



460

Figure 8: Temporal evolutions of the three indicators for the three forest sites (FR-Hes, DE-Hai, DK-Sor). Each panel corresponds to a different GPP indicator: initial slope (IRise, top), peaking values (IPeak, middle) and mid-season drop intensity (IDrop, bottom). Data points represent observed annual values for each indicator. When site-specific slopes were significant ($p \leq 0.05$), linear trends (solid line) alongside 95 % confidence intervals (shaded areas) are displayed.

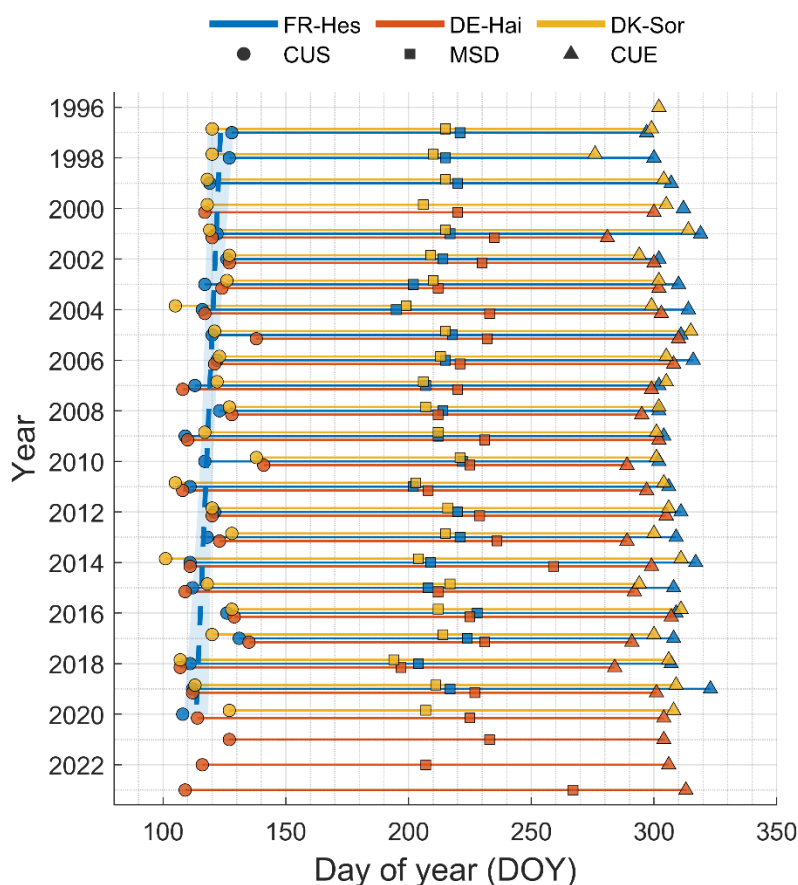
465

IPeak presented a significant Site×Year interaction ($p < 0.001$), meaning that sites differences between sites were time-dependent (as seen in Fig. 8). DK-Sor presented by far the fastest increase (slope = 202.1, $p < 0.001$) followed by FR-Hes (slope = 108.5, $p < 0.001$). On the other hand, IPeak values at DE-Hai decreased over years (slope = -114.2, $p < 0.001$). These dynamics lead to inter-site differences widening over time. Around year 2000, all sites presented similar IPeak values with DE-Hai being the highest by a small margin. By year 2020, GPP peaking values were significantly higher at DK-Sor, FR-Hes being intermediate and DE-Hai being the lowest (Fig. 8). At FR-Hes, LAI and IPeak were strongly correlated ($r = 0.85$, $p < 0.001$).

470

Similar to IRise, no significant Site×Year interaction was observed for IDrop ($p = 0.15$). All three sites presented significantly different EMMs (Table 3). Values were highest at DK-Sor (6.72 ± 1.01), intermediate at FR-Hes (5.55 ± 1.04) and lowest at DE-Hai (4.10 ± 1.03), although DK-Sor presented no years with exceptional mid-season drop intensity contrary to the other two sites (Fig. 8). No significant temporal trend was detected for either site.

3.4 Phenology



475

Figure 9: Phenological markers for the three forest sites (FR-Hes, DE-Hai and DK-Sor). Years are displayed on the vertical axis (in reversed chronological order) and day of year (DOY) on the horizontal axis. Marker shape differentiates three phenological events: carbon uptake start (CUS, circle), mid-season drop (MSD, square) or carbon uptake end (CUE, triangle). Horizontal segments connect events within each year. Linear temporal trends are shown (in dashed lines) only when the regression slope is statistically significant ($p \leq 0.05$). Shaded bands represent 95% confidence intervals around significant regression lines.

480

Across all phenological markers, no significant Site×Year interaction was detected (Table 3), indicating that phenological differences among sites were consistent through time. Site effects can therefore be interpreted as overall differences in phenology, independent of temporal trends.

485

Pairwise comparisons of EMM showed no significant differences in the CUS among sites. In contrast, the end of the carbon uptake period differed significantly between all three sites. DE-Hai exhibited the earliest CUE, followed by DK-Sor ($\Delta = 5.29$ days, $p = 0.0048$) and FR-Hes ($\Delta = 11$ days, $p < 0.001$). In consequence, CUL was significantly shorter at DE-Hai than at DK-Sor ($\Delta = 6.37$ days, $p = 0.011$) and at DK-Sor than at FR-Hes ($\Delta = 6.5$ days, $p = 0.0087$).

MSD occurred significantly later at DE-Hai than at both FR-Hes ($\Delta = 11.8$ days, $p < 0.001$) and DK-Sor ($\Delta = 15.5$ days, $p < 0.001$). The latter two sites did not differ significantly in mid-season drop timing.



490 A significant long-term trend was observed at FR-Hes (Fig. 9), where CUS advanced over time (slope = -0.43 days yr^{-1} , $p = 0.030$). Temporal trends suggested a slight lengthening of CUL at DE-Hai (slope = 0.52 days yr^{-1} , $p = 0.18$), DK-Sor (slope = 0.50 days yr^{-1} , $p = 0.18$) and FR-Hes (slope = 0.73 days yr^{-1} , $p = 0.027$), but the trend was significant only at the latter site. No significant temporal trends were detected for other sites and metrics.

Correlations between indicators and between indicators and phenological markers were almost all non-significant. Interestingly, IRise showed a significant negative correlation with the mid-season drop date relative to CUS at FR-Hes ($r = -0.59$, $p = 0.005$) and at DE-Hai ($r = -0.74$, $p < 0.001$), suggesting that later GPP drops within the season are associated with lower spring GPP rise rates. A similar relationship was observed at DK-Sor ($r = -0.33$, $p = 0.12$), although non-significant. Nonetheless, this relationship becomes significant using the reference CUS ($r = -0.67$, $p < 0.001$) although relationships for other sites did not change, hinting to the difficulty of identifying phenological markers at DK-Sor using the GPP signal.

500 4 Discussion

4.1 Performance and robustness of indicators and phenological dates

Benchmarking against GPP “reference” values shows strong overall agreement, with IPeak and IRise exhibiting higher concordance than IDrop. This hierarchy is mechanistically intuitive: peak-season GPP is typically characterized by strong signal-to-noise ratio, while mid-season features (the drop) integrate multiple interacting stressors (e.g. vapor pressure deficit, soil moisture limitation, heat) and are therefore both more variable and more method-sensitive (Panwar et al., 2023; Rukh et al., 2023). Similarly, MSD is the most difficult phenological marker to recover robustly, with lower correlations and large potential shifts relative to smoothed GPP reference dates (up to 40 days). This is not surprising as mid-season “drop” is an emergent property of episodic stress, and thus it depends strongly on how the seasonal curve is smoothed and how “drop” is operationally defined.

510 The generally lower correlations of phenological markers at DK-Sor reflect the smoother spring and autumn transitions of GPP at this site. This is consistent with the stand’s managed and relatively even-aged structure, as well as with the milder, maritime climate, which tends to produce more gradual seasonal transitions (Pilegaard and Ibrom, 2020).

4.2 Contrasting annual carbon balances across sites

Across the three temperate forest sites, the NEE is consistently negative (net sinks), but the magnitude and direction of temporal change differ markedly. The fact that interannual and long-term variations in NEE track GPP more strongly than aligns with broader eddy-covariance evidence that productivity metrics tend to show stronger sensitivity to interannual variability and long-term change than ecosystem respiration (Baldocchi et al., 2018; Moreaux et al., 2020). Reco remains comparatively buffered because it is distributed across heterogeneous organ and microbial sources and constrained by substrate availability (Granier et al., 2008; Ngao et al., 2012).



520 The declining annual GPP at DE-Hai is consistent with mechanisms proposed for age- or size-related declines in forest
production, where increasing tree height/size can introduce hydraulic limitations, reduce stomatal conductance, and depress
photosynthesis, even if respiration does not increase proportionally (Drake et al., 2011). These mechanisms can operate at
stand scale even when structural heterogeneity is high, as in old forests (Genet et al., 2010; Hesse et al., 2023). Conversely,
increasing GPP at DK-Sor and FR-Hes is consistent with managed stand dynamics: thinning can sustain or enhance canopy
525 light distribution and maintain higher assimilation capacity per unit leaf area, while stand development in younger/maturing
forests can still be on the rising limb of productivity (Granier et al., 2008). Furthermore, frequent thinning enhances tree
performance during drought by increasing soil water availability, reducing stand-level transpiration, and sustaining higher
radial growth before, during, and after drought events (Sohn et al., 2016). These interpretations are consistent with long-term
FR-Hes and DK-Sor records, which report increasing net CO₂ uptake and persistent flux-phenology relationships (Granier et
530 al., 2008; Pilegaard et al., 2011).

4.3 Inter-site differences in indicators and phenology

The rate of increase in GPP (IRise), significantly higher at FR-Hes than at DE-Hai or DK-Sor, suggests a more rapid spring
activation of photosynthesis in this relatively young beech-dominated stand. Nonetheless, IRise has significantly declined at
FR-Hes over the study period. Concurrently, the CUS has advanced by approximately 0.43 days per year, a rate slightly
535 higher than previously reported for European beech stands (Schwartz et al., 2006; Skvareninova et al., 2024). These two
trends are interconnected: an earlier CUS extends the time available to reach peak GPP, typically occurring near the summer
solstice (median dates of 14 June, 21 June and 22 June resp. for DK-Sor, DE-Hai and FR-Hes). Consequently, peak
productivity is reached later in the GS, resulting in a slower overall GPP growth rate.

This advancement in bud burst has been widely documented across beech stands in various climates and elevations
540 (Bednářová et al., 2014; Fu et al., 2018; Prislán et al., 2019; Skvareninova et al., 2024; Stagakis et al., 2022). It is
particularly pronounced in cooler climates and at higher altitudes, where beech phenology is more strongly regulated by
temperature than photoperiod (Vitasse and Basler, 2013). In contrast, in warmer regions, photoperiod exerts a greater
influence on spring phenology, offering a more stable seasonal cue than temperature, which is subject to local variability and
extremes (Basler and Körner, 2012). Despite its mild climate and low elevation, the FR-Hes site exhibits a pronounced
545 advancement in CUS (Prislán et al., 2019; Skvareninova et al., 2024; Vitasse and Basler, 2013), suggesting a strong
temperature sensitivity in bud burst timing which contributes to the observed decline in IRise. The trend may be further
amplified by the temperature dependency of bud development rates (Basler and Körner, 2014). However, the long-term
trajectory of IRise remains uncertain, as beech at FR-Hes may adapt to warming by increasing its reliance on photoperiod to
regulate ecodormancy release (Basler and Körner, 2012; Fu et al., 2015). Additionally, pre-summer temperatures enhance
550 IRise, which could partially offset the negative impact of earlier CUS on IRise. This compensatory effect may be moderated
by two factors: (1) structural changes in the stand, as the FR-Hes beech stand presents an increased basal area and reduced
tree density, which enhances LAI development (Bequet et al., 2011), and (2) shifts in the species composition, with a rising



555 proportion of hornbeam and oak, species that exhibit respectively earlier and later leaf-out compared to beech (Zahnd et al., 2023). Nevertheless, no clear changes in IRise or CUS were observed following thinning, suggesting that the influence of species composition shifts remains limited.

560 IPeak shows both strong site differences and divergent temporal trajectories, with DK-Sor increasing most rapidly, FR-Hes increasing moderately, and DE-Hai decreasing. Explanations are most likely multifactorial as peak GPP integrates canopy capacity (leaf area, nitrogen status, light distribution), physiological constraints (stomatal regulation under VPD), and stand structure. For DE-Hai, the decline in IPeak aligns with expectations for an aging, unmanaged system where hydraulic limitations, competition, and structural senescence can reduce maximum canopy conductance and assimilation capacity (Drake et al., 2011). At FR-Hes, the forest experienced consistent biomass accumulation and canopy expansion, enhancing photon capture and CO₂ assimilation. IPeak therefore correlates strongly with LAI, a key driver of productivity (Le Dantec et al., 2000). In parallel, atmospheric CO₂ concentrations rose significantly at all sites. Elevated CO₂ concentrations enhances GPP by increasing substrate availability at Rubisco's catalytic site (Jiang et al., 2020; Stitt, 1991). Free-Air CO₂ 565 Enrichment experiments and modelling studies have demonstrated that elevated CO₂ can also increase LAI by modifying crown architecture and promoting carbon allocation to shaded leaves (McCarthy et al., 2007; Norby and Zak, 2011). The observed correlation between CO₂ concentrations and LAI supports this hypothesis, although their relationship remains complex and is constrained by resource availability (Duursma et al., 2016). Furthermore, evidence of this effect is still scarce and most apparent in stands with low LAI (Norby and Zak, 2011).

570 IDrop shows no consistent temporal trend at all sites. This variability is expected, as IDrop is primarily influenced by meteorological conditions during the growing season, particularly aerial and edaphic drought (Wankmüller et al., 2024). Beeches are known to show strong physiological sensitivity to drought and heat, including stomatal closure, reduced photosynthesis, and, during severe events, early senescence or canopy damage (Bréda et al., 2006; Leuschner, 2020). Large reductions in beech vitality and productivity have been reported during drought across Central Europe, with legacy effects 575 and increased vulnerability to subsequent stressors (Rukh et al., 2023; Thomas et al., 2024). While drought frequency has increased in recent years, its intensity remains irregular, preventing the emergence of a monotonic trend.

Nonetheless, IDrop differs consistently among sites, indicating that the magnitude of mid-season reductions in photosynthesis represents a stable site-specific property. The unmanaged old-growth stand at DE-Hai displayed the lowest mid-season declines. This summer stability is consistent with features typical of unmanaged old-growth beech forests, i.e. 580 deep and spatially heterogeneous rooting systems, multilayered canopies that buffer radiation and vapor pressure deficit, and a conservative water-use strategy that can mitigate short-term summer stress (Adhikari et al., 2025; Genet et al., 2010; Yu et al., 2022). In contrast, DK-Sor exhibited the highest IDrop values, reflecting stronger mid-season reductions in GPP. The stand's vertically concentrated canopy combined with high exposure to atmospheric conditions, likely amplifies summer constraints by producing a large proportion of leaves at the canopy top, where heat load and vapor pressure deficit are 585 maximal (Bachofen et al., 2020; Pilegaard et al., 2003). Despite these larger reductions, DK-Sor also showed the lowest interannual variability in IDrop, suggesting that while mid-season declines are more pronounced, they occur with greater

year-to-year consistency, reflecting the stability of its maritime climate (Chiesi et al., 2016; Pilegaard and Ibrom, 2020). FR-Hes showed intermediate values with large variability, consistent with its mixed management history, the more constrained hydrology of its luvisol/stagnic luvisol soils and its partially shifting species composition.

590 The absence of significant Site×Year interactions for all phenological markers implies that site differences in phenology have remained stable over time, despite ongoing climate change. CUS is remarkably similar among sites, suggesting that spring phenology is largely driven by regional climate rather than by stand structure or age. In contrast, CUE (and the overall CUL) differs significantly across sites, implying stronger influence of local stresses and stand properties. At DE-Hai, the earlier CUE suggests that late-season carbon assimilation is constrained, most likely by the forest’s structural and
595 physiological characteristics (Herbst et al., 2015). DE-Hai is an uneven-aged, old-growth stand where mature trees experience stronger hydraulic limitations and higher respiration costs (Curtis and Gough, 2018), making them more vulnerable to stress-induced declines in late-season productivity. In contrast, FR-Hes exhibits the latest CUE and the longest CUL. Although no direct evidence exists that younger stands systematically delay the end of the growing season, younger and fast-growing trees are known to show greater phenological plasticity and higher photosynthetic capacity per unit leaf
600 area, which can translate into extended activity under favorable conditions (Vitasse, 2013). At this site, senescence timing has been shown to be a primary driver of interannual variability in CUL and GPP, with later senescence strongly associated with higher productivity (Granier et al., 2008). These features provide a plausible physiological basis for the prolonged carbon-active season observed at FR-Hes, even if autumn phenology drivers (including age effects) remain insufficiently quantified in current literature (Silvestro et al., 2025).

605 The negative correlation between IRise and the timing of the mid-season drop suggests a potential intra-seasonal trade-off: faster early-season development, driven by accelerated leaf expansion, leads to an earlier, though not necessarily more pronounced, decline in GPP. This pattern suggests a coupling between spring and autumn phenophases, where rapid spring development may trigger earlier senescence. Similar relationships have been observed across temperate and boreal forests (Zohner et al., 2023). They likely result from early-season warming, which accelerates leaf development but also promotes
610 faster tissue maturation (Zani et al., 2020), hormonal changes (Chen et al., 2022) and downregulation of photosynthesis due to non-structural carbohydrates accumulation (Luo et al., 2024; Tian et al., 2024).

4.4 Interest of the WAI-based approach

The WAI follows directly from the mathematical structure of the CWT, yet its use and potential have, to our knowledge, not been described in scientific literature. This absence likely stems from historical perspectives: wavelet analysis has long been
615 framed as a spectral tool derived from the FT (Debnath and Shah, 2015), and the intuitive “frequency-oriented” interpretation of Fourier coefficients was simply transferred to wavelets. As a result, alternative ways of interpreting individual wavelet coefficients have rarely been explored. In addition, applying WAI in practice requires selecting specific coefficients from the large number produced by the transform, and its interpretations depend on the shape of the chosen wavelet. These factors make WAI difficult to use as a standalone analysis tool. By embedding WAI within the structured



620 3-step workflow introduced in this study, coefficient selection becomes systematic, wavelet dependence becomes explicit and interpretable, and the method becomes reproducible and accessible to non-specialists. In this integrated form, WAI operates as a practical extension of wavelet analysis, enabling meaningful ecological interpretations of seasonal carbon-cycle patterns.

The WAI-based approach expands the information typically extracted from scalograms. Whereas classical wavelet analyses focus primarily on dominant patterns (i.e. local maxima in coefficient amplitude), examining peak distributions within period bands provides a systematic view of recurrent behaviors in the signal. This procedure highlights both regular seasonal features and irregularities, such as missing or isolated peaks, and greatly enlarges the set of wavelet coefficients that can be meaningfully interpreted. The WAI then links each selected coefficient to its contributing areas, enabling direct interpretation without relying on significance testing, although statistical tools can still assist in guiding exploration.

630 Although different wavelets may emphasize different structures, the DOG2 wavelet generally offers a robust starting point for ecological applications due to its stability in detecting peaks and trend discontinuities.

This broader interpretative capacity makes it possible to construct various indicators that closely match specific signal features. While some metrics could theoretically be approximated by simpler measures (e.g. numerical slopes for IRise), such substitutions lack the versatility and sensitivity of the WAI approach. Crucially, the dates identified from period-band peaks determine the temporal windows used for indicator calculation, removing the need to define external positioning criteria. The method also avoids explicit signal manipulation: no smoothing, thresholds, or curve fitting are required. This is particularly valuable because choices in smoothing or thresholding can shift phenological transition estimates by weeks, with uncertainties especially large near transitional periods where the GPP signal is weakest or most complex (Panwar et al., 2023). These considerations are central for defining the MSD, which is often not a discrete event but an emergent property of episodic stress.

640

Finally, WAI offers practical advantages for working with real-world ecological data. Like Fourier-based approaches, CWT assumes continuous, regularly spaced inputs, which is rarely met in environmental records. By targeting specific coefficients, the WAI limits this requirement to the wavelet support, allowing small gaps within that interval to be handled using local gap-filling without altering the broader analysis. Nonetheless, indicator stability still depends on data quality, and large gaps or low-quality periods can influence results. Within these constraints, however, the WAI-based workflow provides a robust, reproducible, and flexible way to extract ecologically meaningful information from complex time-series.

645

4.5 Perspectives in ecology

A key strength of the WAI-based 3-step approach is its ability to detect recurring patterns even when the spacing between events is irregular. Because the method operates on the distribution and structure of wavelet coefficients, it can identify repeated behaviors regardless of their periodicity or strength. This property is particularly valuable for ecological applications in which seasonal dynamics are weak, episodic or highly variable across years. Tropical ecosystems, for instance, often exhibit aseasonal or event-driven productivity pulses, or shorter and less predictable growing seasons

650



655 compared to temperate forests (Reich, 1995). While Fourier-based analyses have been used to describe such flexible
cyclicality (Bush et al., 2017), they do not provide temporal localization of events. By contrast, the WAI approach naturally
accommodates these systems, allowing both the timing and the strength of recurrent features to be compared across periods.
Beyond identifying patterns, the indicator framework enables direct comparison of signals through a small, interpretable set
of metrics. Indicators summarize the behavior of specific signal features, allowing comparisons among sites, ecosystems or
experimental treatments without relying on full time-series inspection. This is particularly valuable for multi-site analyses,
where similar processes may express differently depending on local constraints. The approach also provides a practical tool
660 for model evaluation: discrepancies between observed and simulated indicators highlight which aspects of ecosystem
dynamics are well or poorly represented in the model.

Linking indicators to environmental drivers offers another promising direction. Long-term ecological studies often rely on
broad annual metrics, such as sums (Baldocchi et al., 2018) or anomalies (Aubinet et al., 2018), or multiscale methods, such
as time-series decomposition (Wu et al., 2012), random forests (Moreaux et al., 2020), or wavelet decomposition (Sturtevant
665 et al., 2016). Because indicators isolate specific signal features, their correlations with drivers provide a complementary lens,
by revealing localized and process-specific influences that are not captured by aggregated metrics. This can enhance our
understanding of ecosystem-atmosphere interactions, stress responses, and population or community dynamics, and
ultimately improve model parameterization. Exploring these relationships is the focus of the companion paper (second part
of this study), which examines how indicator-driver linkages elucidate the mechanisms underlying interannual GPP
670 variability.

The WAI-based date selection approach also opens new possibilities for phenological research. Metrics such as canopy
development, senescence timing or growing-season boundaries are typically derived from smoothed vegetation indices and
threshold- or derivative-based methods (Caparros-Santiago et al., 2021). Our method avoids assumptions about curve shape
and does not require smoothing, as dates arise directly from discontinuity detection in the signal. This ensures
675 period-specific adaptation and improves robustness when dealing with complex or noisy seasonal transitions. However,
performance still depends on data quality and on selecting an appropriate wavelet, since inadequate choices can obscure
subtle or short-lived events. WAI visualization offers a practical way to guide these decisions.

Finally, the WAI framework could be extended to bivariate wavelet tools such as the cross-wavelet transform or wavelet
coherence, which examine relationships between variables (Cazelles et al., 2008). These methods are powerful but limited
680 when analyzing delayed effects, because their usable lag range is constrained by the wavelet support, shape and complex/real
nature. Ecological studies give increasing attention to delayed effects, particularly in recent years (Aubinet et al., 2018). If
driver-response lags are expected, the indicator-comparison framework provides greater flexibility, as lags can be adjusted
manually within the limits of the dataset.



5 Conclusions

685 This paper introduces a wavelet-based framework that systematically identifies recurrent seasonal events in ecosystem carbon-flux time series. By using the full structure of wavelet coefficients rather than a restricted set of significant power regions, the approach provides a flexible and scale-aware foundation for characterizing seasonal dynamics in gross primary productivity. The WAI method enabled the extraction of consistent carbon-uptake phenological markers while the three structural indicators (IRise, IPeak and IDrop) offered complementary information about the timing, magnitude and internal
690 shape of the seasonal GPP cycle. Benchmarking against smoothed-GPP references confirmed the robustness of these indicators, especially for spring rise and peak productivity, while clarifying the expected uncertainty in mid-season metrics.

Applied to long-term eddy-covariance records from three contrasting European beech-dominated forests, the framework revealed clear and ecologically meaningful differences in seasonal structure and long-term carbon-sink trajectories. The unmanaged old-growth forest exhibited declining peak productivity and a shortening effective carbon-uptake period, while
695 the two managed stands showed sustained or increasing productivity, highlighting the combined influence of forest age, management and climate. Across sites, the indicators exposed consistent seasonal contrasts (such as rapid spring activation, variable mid-season resilience, and site-specific end-of-season timing) and uncovered an intra-seasonal trade-off linking strong spring growth to earlier mid-season declines.

Together, these findings demonstrate that the proposed wavelet-based approach provides a powerful and general tool for
700 extracting ecological information from noisy, non-stationary signals. It opens new avenues for understanding how seasonal processes scale to long-term carbon-sink dynamics, and how forest responses to climate and management evolve across decades. As long-term flux networks continue to expand, such tools will be increasingly valuable for diagnosing ecosystem change and improving predictions of forest carbon dynamics under future climate conditions.

Code and data availability

705 The WAI code and FR-Hes data used for this study are openly available on GitHub at <https://github.com/jonathanbitton/Wavelet-WAI>. A permanent archived version is available through Zenodo at <https://doi.org/10.5281/zenodo.19207876>.

Data from DE-Hai (<https://doi.org/11676/rOKIh2gg8tEEExEelC67ZCp9q>) and DK-Sor (<https://doi.org/10.18160/X4DF-R4S2>) are publicly available through the ICOS Carbon Portal.

710 Author contributions

JB: Conceptualization, Methodology, Formal analysis, Software, Data Curation, Writing - Original Draft, Visualization. BL: Conceptualization, Methodology, Formal analysis, Data Curation, Resources, Writing - Review & Editing, Supervision, Project administration. CC: Conceptualization, Methodology, Formal analysis, Writing - Review & Editing, Supervision,



Project administration. BH: Conceptualization, Methodology, Formal analysis, Writing - Review & Editing, Supervision,
715 Project administration.

Competing interests

The authors declare that they have no conflict of interest.

Acknowledgements

The authors gratefully acknowledge the support of the Integrated Carbon Observation System (ICOS) research infrastructure
720 for providing continuous high-quality observations essential to this study. We thank the teams operating the ICOS ecosystem
stations DE-Hai (Principal Investigator: Alexander Knohl), DK-Sor (Principal Investigator: Andreas Ibrom), and FR-Hes
(Principal Investigator: Matthias Cuntz) for their dedicated work in maintaining the sites, ensuring data quality, and
facilitating access to long-term measurements. We also thank Adeline Fayolle, Aurore Brut and Samuel Nicolay for their
continuous guidance and feedback on the research project.

725 Financial support

The researchers were funded by the Fédération Wallonie-Bruxelles.

References

- Abbate, A., DeCusatis, C. M., and Das, P. K.: Wavelets and Subbands, Birkhäuser, Boston, MA,
<https://doi.org/10.1007/978-1-4612-0113-7>, 2002.
- 730 Adhikari, Y., Blumröder, J. S., Meier, C., and Ibisch, P. L.: Beech buffers: Microclimate regulation in temperate old-growth
forests, surroundings and forest edge, *Ecol. Indic.*, 178, 114111, <https://doi.org/10.1016/j.ecolind.2025.114111>, 2025.
- Allan, B. M., Nimmo, D. G., Ierodiaconou, D., VanDerWal, J., Koh, L. P., and Ritchie, E. G.: Futurecasting ecological
research: the rise of technoecology, *Ecosphere*, 9, e02163, <https://doi.org/10.1002/ecs2.2163>, 2018.
- 735 Ascough, J. C., Maier, H. R., Ravalico, J. K., and Strudley, M. W.: Future research challenges for incorporation of
uncertainty in environmental and ecological decision-making, *Ecol. Model.*, 219, 383–399,
<https://doi.org/10.1016/j.ecolmodel.2008.07.015>, 2008.
- Aubinet, M., Vesala, T., and Papale, D. (Eds.): *Eddy Covariance: A Practical Guide to Measurement and Data Analysis*,
Springer Netherlands, Dordrecht, <https://doi.org/10.1007/978-94-007-2351-1>, 2012.
- 740 Aubinet, M., Hurdebise, Q., Chopin, H., Debacq, A., De Ligne, A., Heinesch, B., Manise, T., and Vincke, C.: Inter-annual
variability of Net Ecosystem Productivity for a temperate mixed forest: A predominance of carry-over effects?, *Agric. For.
Meteorol.*, 262, 340–353, <https://doi.org/10.1016/j.agrformet.2018.07.024>, 2018.



- Bachofen, C., D'Odorico, P., and Buchmann, N.: Light and VPD gradients drive foliar nitrogen partitioning and photosynthesis in the canopy of European beech and silver fir, *Oecologia*, 192, 323–339, <https://doi.org/10.1007/s00442-019-04583-x>, 2020.
- 745 Baldocchi, D., Chu, H., and Reichstein, M.: Inter-annual variability of net and gross ecosystem carbon fluxes: A review, *Agric. For. Meteorol.*, 249, 520–533, <https://doi.org/10.1016/j.agrformet.2017.05.015>, 2018.
- Basler, D. and Körner, C.: Photoperiod sensitivity of bud burst in 14 temperate forest tree species, *Agric. For. Meteorol.*, 165, 73–81, <https://doi.org/10.1016/j.agrformet.2012.06.001>, 2012.
- 750 Basler, D. and Körner, C.: Photoperiod and temperature responses of bud swelling and bud burst in four temperate forest tree species, *Tree Physiol.*, 34, 377–388, <https://doi.org/10.1093/treephys/tpu021>, 2014.
- Bednářová, E., Kučera, J., and Merkllová, L.: The onset and duration of vegetative phenological stages in European beech (*Fagus sylvatica* L.) under changing conditions of the environment, *Acta Univ. Agric. Silvic. Mendel. Brun.*, 58, 23–30, <https://doi.org/10.11118/actaun201058040023>, 2014.
- 755 Bequet, R., Campioli, M., Kint, V., Vansteenkiste, D., Muys, B., and Ceulemans, R.: Leaf area index development in temperate oak and beech forests is driven by stand characteristics and weather conditions, *Trees*, 25, 935–946, <https://doi.org/10.1007/s00468-011-0568-4>, 2011.
- Bracewell, R. N.: *The Fourier Transform and Its Applications*, McGraw Hill, 2000.
- 760 Bréda, N., Huc, R., Granier, A., and Dreyer, E.: Temperate forest trees and stands under severe drought: a review of ecophysiological responses, adaptation processes and long-term consequences, *Ann. For. Sci.*, 63, 625–644, <https://doi.org/10.1051/forest:2006042>, 2006.
- Bush, E. R., Abernethy, K. A., Jeffery, K., Tutin, C., White, L., Dimoto, E., Dikangadissi, J.-T., Jump, A. S., and Bunnefeld, N.: Fourier analysis to detect phenological cycles using long-term tropical field data and simulations, *Methods Ecol. Evol.*, 8, 530–540, <https://doi.org/10.1111/2041-210X.12704>, 2017.
- 765 Campioli, M., Gielen, B., Göckede, M., Papale, D., Bouriaud, O., and Granier, A.: Temporal variability of the NPP-GPP ratio at seasonal and interannual time scales in a temperate beech forest, *Biogeosciences*, 8, 2481–2492, <https://doi.org/10.5194/bg-8-2481-2011>, 2011.
- Caparros-Santiago, J. A., Rodriguez-Galiano, V., and Dash, J.: Land surface phenology as indicator of global terrestrial ecosystem dynamics: A systematic review, *ISPRS J. Photogramm. Remote Sens.*, 171, 330–347, <https://doi.org/10.1016/j.isprsjprs.2020.11.019>, 2021.
- 770 Carl, G., Doktor, D., Koslowsky, D., and Kühn, I.: Phase difference analysis of temperature and vegetation phenology for beech forest: a wavelet approach, *Stoch. Environ. Res. Risk Assess.*, 27, 1221–1230, <https://doi.org/10.1007/s00477-012-0658-x>, 2013.
- Cazelles, B., Chavez, M., Berteaux, D., Ménard, F., Vik, J. O., Jenouvrier, S., and Stenseth, N. C.: Wavelet analysis of ecological time series, *Oecologia*, 156, 287–304, <https://doi.org/10.1007/s00442-008-0993-2>, 2008.
- 775 Cazelles, B., Cazelles, K., and Chavez, M.: Wavelet analysis in ecology and epidemiology: impact of statistical tests, *J. R. Soc. Interface*, 11, 20130585, <https://doi.org/10.1098/rsif.2013.0585>, 2014.



- Chen, Q., Zhang, J., and Li, G.: Dynamic epigenetic modifications in plant sugar signal transduction, *Trends Plant Sci.*, 27, 379–390, <https://doi.org/10.1016/j.tplants.2021.10.009>, 2022.
- 780 Chiesi, M., Chirici, G., Marchetti, M., Hasenauer, H., Moreno, A., Knohl, A., Matteucci, G., Pilegaard, K., Granier, A., Longdoz, B., and Maselli, F.: Testing the applicability of BIOME-BGC to simulate beech gross primary production in Europe using a new continental weather dataset, *Ann. For. Sci.*, 73, 713–727, <https://doi.org/10.1007/s13595-016-0560-7>, 2016.
- Cuntz, M., Longdoz, B., ICOS Ecosystem Thematic Centre, ICOS Ecosystem Thematic Centre, and Trotta, C.: Warm winter 2020 ecosystem eddy covariance flux product from Hesse (1.0), <https://doi.org/10.18160/GFQX-22T7>, 2021.
- 785 Curtis, P. S. and Gough, C. M.: Forest aging, disturbance and the carbon cycle, *New Phytol.*, 219, 1188–1193, <https://doi.org/10.1111/nph.15227>, 2018.
- Debnath, L. and Shah, F. A.: *Wavelet Transforms and Their Applications*, Birkhäuser, Boston, MA, <https://doi.org/10.1007/978-0-8176-8418-1>, 2015.
- Dellwik, E. and Jensen, N. O.: Flux–Profile Relationships Over a Fetch Limited Beech Forest, *Bound.-Layer Meteorol.*, 115, 790 179–204, <https://doi.org/10.1007/s10546-004-3808-y>, 2005.
- Drake, J. E., Davis, S. C., Raetz, L. M., and DeLUCIA, E. H.: Mechanisms of age-related changes in forest production: the influence of physiological and successional changes, *Glob. Change Biol.*, 17, 1522–1535, <https://doi.org/10.1111/j.1365-2486.2010.02342.x>, 2011.
- 795 Duursma, R. A., Gimeno, T. E., Boer, M. M., Crous, K. Y., Tjoelker, M. G., and Ellsworth, D. S.: Canopy leaf area of a mature evergreen Eucalyptus woodland does not respond to elevated atmospheric [CO₂] but tracks water availability, *Glob. Change Biol.*, 22, 1666–1676, <https://doi.org/10.1111/gcb.13151>, 2016.
- Farge, M.: Wavelet Transforms and Their Applications to Turbulence, *Annu. Rev. Fluid Mech.*, 24, 395–458, <https://doi.org/10.1146/annurev.fl.24.010192.002143>, 1992.
- 800 Fu, Y. H., Zhao, H., Piao, S., Peaucelle, M., Peng, S., Zhou, G., Ciais, P., Huang, M., Menzel, A., Peñuelas, J., Song, Y., Vitasse, Y., Zeng, Z., and Janssens, I. A.: Declining global warming effects on the phenology of spring leaf unfolding, *Nature*, 526, 104–107, <https://doi.org/10.1038/nature15402>, 2015.
- Fu, Y. H., Piao, S., Delpierre, N., Hao, F., Hänninen, H., Liu, Y., Sun, W., Janssens, I. A., and Campioli, M.: Larger temperature response of autumn leaf senescence than spring leaf-out phenology, *Glob. Change Biol.*, 24, 2159–2168, <https://doi.org/10.1111/gcb.14021>, 2018.
- 805 Genet, H., Bréda, N., and Dufrêne, E.: Age-related variation in carbon allocation at tree and stand scales in beech (*Fagus sylvatica* L.) and sessile oak (*Quercus petraea* (Matt.) Liebl.) using a chronosequence approach, *Tree Physiol.*, 30, 177–192, <https://doi.org/10.1093/treephys/tpp105>, 2010.
- Gennaretti, F., Ogée, J., Sainte-Marie, J., and Cuntz, M.: Mining ecophysiological responses of European beech ecosystems to drought, *Agric. For. Meteorol.*, 280, 107780, <https://doi.org/10.1016/j.agrformet.2019.107780>, 2020.
- 810 Granier, A., Bréda, N., Longdoz, B., Gross, P., and Ngao, J.: Ten years of fluxes and stand growth in a young beech forest at Hesse, North-eastern France, *Ann. For. Sci.*, 65, 704–704, <https://doi.org/10.1051/forest:2008052>, 2008.



- Herbst, M., Mund, M., Tamrakar, R., and Knohl, A.: Differences in carbon uptake and water use between a managed and an unmanaged beech forest in central Germany, *For. Ecol. Manag.*, 355, 101–108, <https://doi.org/10.1016/j.foreco.2015.05.034>, 2015.
- 815 Hesse, B. D., Gebhardt, T., Hafner, B. D., Hikino, K., Reitsam, A., Gigl, M., Dawid, C., Häberle, K.-H., and Grams, T. E. E.: Physiological recovery of tree water relations upon drought release—response of mature beech and spruce after five years of recurrent summer drought, *Tree Physiol.*, 43, 522–538, <https://doi.org/10.1093/treephys/tpac135>, 2023.
- Hudson, I. L., Keatley, M. R., and Kang, I.: Wavelet characterization of eucalypt flowering and the influence of climate, *Environ. Ecol. Stat.*, 18, 513–533, <https://doi.org/10.1007/s10651-010-0149-5>, 2011.
- 820 Ibrom, A., Pilegaard, K., ICOS Ecosystem Thematic Centre, ICOS Ecosystem Thematic Centre, and Trotta, C.: Warm winter 2020 ecosystem eddy covariance flux product from Soroe (1.0), <https://doi.org/10.18160/X4DF-R4S2>, 2022.
- Jiang, M., Medlyn, B. E., Drake, J. E., Duursma, R. A., Anderson, I. C., Barton, C. V. M., Boer, M. M., Carrillo, Y., Castañeda-Gómez, L., Collins, L., Crous, K. Y., De Kauwe, M. G., dos Santos, B. M., Emmerson, K. M., Facey, S. L., Gherlenda, A. N., Gimeno, T. E., Hasegawa, S., Johnson, S. N., Kännaste, A., Macdonald, C. A., Mahmud, K., Moore, B. D., Nazaries, L., Neilson, E. H. J., Nielsen, U. N., Niinemets, Ü., Noh, N. J., Ochoa-Hueso, R., Pathare, V. S., Pendall, E., Pihlblad, J., Piñeiro, J., Powell, J. R., Power, S. A., Reich, P. B., Renchon, A. A., Riegler, M., Rinnan, R., Rymer, P. D., Salomón, R. L., Singh, B. K., Smith, B., Tjoelker, M. G., Walker, J. K. M., Wujeska-Klaue, A., Yang, J., Zaehle, S., and Ellsworth, D. S.: The fate of carbon in a mature forest under carbon dioxide enrichment, *Nature*, 580, 227–231, <https://doi.org/10.1038/s41586-020-2128-9>, 2020.
- 830 Knohl, A., Tiedemann, F., Klosterhalfen, A., Markwitz, C., Fellert, D., Herbst, M., Kolle, O., Kreilein, H., Kutsch, W., Kutsch, W., Rebmann, C., Rebmann, C., and Siebicke, L.: Fluxnet Archive Product from Hainich, 2000–2024, <https://doi.org/11676/rOKIh2gg8tEEeEelC67ZCp9q>, 2025.
- Krapivin, V. F. and Shutko, A. M.: *Information Technologies for Remote Monitoring of the Environment*, Springer, Berlin, Heidelberg, <https://doi.org/10.1007/978-3-642-20567-5>, 2012.
- 835 Krapivin, V. F., Varotsos, C. A., and Soldatov, V. Yu.: *New Ecoinformatics Tools in Environmental Science: Applications and Decision-making*, Springer International Publishing, Cham, <https://doi.org/10.1007/978-3-319-13978-4>, 2015.
- Kulla, L., Roessiger, J., Bošefa, M., Kucbel, S., Murgaš, V., Vencurik, J., Pittner, J., Jaloviar, P., Šumichrast, L., and Saniga, M.: Changing patterns of natural dynamics in old-growth European beech (*Fagus sylvatica* L.) forests can inspire forest management in Central Europe, *For. Ecol. Manag.*, 529, 120633, <https://doi.org/10.1016/j.foreco.2022.120633>, 2023.
- 840 Le Dantec, V., Dufrêne, E., and Saugier, B.: Interannual and spatial variation in maximum leaf area index of temperate deciduous stands, *For. Ecol. Manag.*, 134, 71–81, [https://doi.org/10.1016/S0378-1127\(99\)00246-7](https://doi.org/10.1016/S0378-1127(99)00246-7), 2000.
- Leuschner, C.: Drought response of European beech (*Fagus sylvatica* L.)—A review, *Perspect. Plant Ecol. Evol. Syst.*, 47, 125576, <https://doi.org/10.1016/j.ppees.2020.125576>, 2020.
- 845 Luo, Y., Zohner, C., Crowther, T. W., Feng, J., Hoch, G., Li, P., Richardson, A. D., Vitasse, Y., and Gessler, A.: Internal physiological drivers of leaf development in trees: Understanding the relationship between non-structural carbohydrates and leaf phenology, *Funct. Ecol.*, n/a, 1–14, <https://doi.org/10.1111/1365-2435.14694>, 2024.
- Mallat, S. (Ed.): *A Wavelet Tour of Signal Processing, Third Edition.*, Academic Press, Boston, <https://doi.org/10.1016/B978-0-12-374370-1.50001-9>, 2009.



- 850 Marvin, D. C., Koh, L. P., Lynam, A. J., Wich, S., Davies, A. B., Krishnamurthy, R., Stokes, E., Starkey, R., and Asner, G. P.: Integrating technologies for scalable ecology and conservation, *Glob. Ecol. Conserv.*, 7, 262–275, <https://doi.org/10.1016/j.gecco.2016.07.002>, 2016.
- McCarthy, H. R., Oren, R., Finzi, A. C., Ellsworth, D. S., Kim, H.-S., Johnsen, K. H., and Millar, B.: Temporal dynamics and spatial variability in the enhancement of canopy leaf area under elevated atmospheric CO₂, *Glob. Change Biol.*, 13, 2479–2497, <https://doi.org/10.1111/j.1365-2486.2007.01455.x>, 2007.
- 855 Moffat, A. M., Papale, D., Reichstein, M., Hollinger, D. Y., Richardson, A. D., Barr, A. G., Beckstein, C., Braswell, B. H., Churkina, G., Desai, A. R., Falge, E., Gove, J. H., Heimann, M., Hui, D., Jarvis, A. J., Kattge, J., Noormets, A., and Stauch, V. J.: Comprehensive comparison of gap-filling techniques for eddy covariance net carbon fluxes, *Agric. For. Meteorol.*, 147, 209–232, <https://doi.org/10.1016/j.agrformet.2007.08.011>, 2007.
- 860 Moreaux, V., Longdoz, B., Berveiller, D., Delpierre, N., Dufrière, E., Bonnefond, J.-M., Chipeaux, C., Joffre, R., Limousin, J.-M., Ourcival, J.-M., Klumpp, K., Darsonville, O., Brut, A., Tallec, T., Ceschia, E., Panthou, G., and Loustau, D.: Environmental control of land-atmosphere CO₂ fluxes from temperate ecosystems: a statistical approach based on homogenized time series from five land-use types, *Tellus B Chem. Phys. Meteorol.*, 72, 1–25, <https://doi.org/10.1080/16000889.2020.1784689>, 2020.
- 865 Mund, M., Herbst, M., Knohl, A., Matthäus, B., Schumacher, J., Schall, P., Siebicke, L., Tamrakar, R., and Ammer, C.: It is not just a ‘trade-off’: indications for sink- and source-limitation to vegetative and regenerative growth in an old-growth beech forest, *New Phytol.*, 226, 111–125, <https://doi.org/10.1111/nph.16408>, 2020.
- Ngao, J., Epron, D., Delpierre, N., Bréda, N., Granier, A., and Longdoz, B.: Spatial variability of soil CO₂ efflux linked to soil parameters and ecosystem characteristics in a temperate beech forest, *Agric. For. Meteorol.*, 154–155, 136–146, <https://doi.org/10.1016/j.agrformet.2011.11.003>, 2012.
- 870 Norby, R. J. and Zak, D. R.: Ecological Lessons from Free-Air CO₂ Enrichment (FACE) Experiments, *Annu. Rev. Ecol. Evol. Syst.*, 42, 181–203, <https://doi.org/10.1146/annurev-ecolsys-102209-144647>, 2011.
- Oliveira, S. F., Furlinger, K., and Kranzlmüller, D.: Trends in Computation, Communication and Storage and the Consequences for Data-intensive Science, in: 2012 IEEE 14th International Conference on High Performance Computing and Communication & 2012 IEEE 9th International Conference on Embedded Software and Systems, 2012 IEEE 14th International Conference on High Performance Computing and Communication & 2012 IEEE 9th International Conference on Embedded Software and Systems, 572–579, <https://doi.org/10.1109/HPCC.2012.83>, 2012.
- 875 Pandey, P. C. and Sharma, L. K.: Introduction to Natural Resource Monitoring Using Remote Sensing Technology, John Wiley & Sons, Ltd, <https://doi.org/10.1002/9781119616016>, 2021.
- 880 Panwar, A., Migliavacca, M., Nelson, J. A., Cortés, J., Bastos, A., Forkel, M., and Winkler, A. J.: Methodological challenges and new perspectives of shifting vegetation phenology in eddy covariance data, *Sci. Rep.*, 13, 13885, <https://doi.org/10.1038/s41598-023-41048-x>, 2023.
- Percival, D. B. and Walden, A. T.: Spectral Analysis for Physical Applications, Cambridge University Press, Cambridge, <https://doi.org/10.1017/CBO9780511622762>, 1993.
- 885 Pilegaard, K. and Ibrom, A.: Net carbon ecosystem exchange during 24 years in the Sorø Beech Forest – relations to phenology and climate, *Tellus B Chem. Phys. Meteorol.*, 72, <https://doi.org/10.1080/16000889.2020.1822063>, 2020.



- Pilegaard, K., Mikkelsen, T. N., Beier, C., Jensen, N. O., Ambus, P., and Ro-Poulsen, H.: Field measurements of atmosphere-biosphere interactions in a Danish beech forest, *Boreal Environ. Res.*, 8, 315–333, 2003.
- Pilegaard, K., Ibrom, A., Courtney, M. S., Hummelshøj, P., and Jensen, N. O.: Increasing net CO₂ uptake by a Danish beech forest during the period from 1996 to 2009, *Agric. For. Meteorol.*, 151, 934–946, <https://doi.org/10.1016/j.agrformet.2011.02.013>, 2011.
- 890
- Platt, T. and Denman, K. L.: Spectral Analysis in Ecology, *Annu. Rev. Ecol. Evol. Syst.*, 6, 189–210, <https://doi.org/10.1146/annurev.es.06.110175.001201>, 1975.
- Prislan, P., Gričar, J., Čufar, K., de Luis, M., Merela, M., and Rossi, S.: Growing season and radial growth predicted for *Fagus sylvatica* under climate change, *Clim. Change*, 153, 181–197, <https://doi.org/10.1007/s10584-019-02374-0>, 2019.
- 895
- Reich, P. B.: Phenology of tropical forests: patterns, causes, and consequences, *Can. J. Bot.*, 73, 164–174, <https://doi.org/10.1139/b95-020>, 1995.
- Reichman, O. J., Jones, M. B., and Schildhauer, M. P.: Challenges and Opportunities of Open Data in Ecology, *Science*, 331, 703–705, <https://doi.org/10.1126/science.1197962>, 2011.
- Rukh, S., Sanders, T. G. M., Krüger, I., Schad, T., and Bolte, A.: Distinct Responses of European Beech (*Fagus sylvatica* L.) to Drought Intensity and Length—A Review of the Impacts of the 2003 and 2018–2019 Drought Events in Central Europe, *Forests*, 14, 248, <https://doi.org/10.3390/fl14020248>, 2023.
- 900
- Schaller, C., Göckede, M., and Foken, T.: Flux calculation of short turbulent events; comparison of three methods, *Atmospheric Meas. Tech.*, 10, 869–880, <https://doi.org/10.5194/amt-10-869-2017>, 2017.
- Schwartz, M. D., Ahas, R., and Aasa, A.: Onset of spring starting earlier across the Northern Hemisphere, *Glob. Change Biol.*, 12, 343–351, <https://doi.org/10.1111/j.1365-2486.2005.01097.x>, 2006.
- 905
- Silvestro, R., Deslauriers, A., Prislan, P., Rademacher, T., Rezaie, N., Richardson, A. D., Vitasse, Y., and Rossi, S.: From Roots to Leaves: Tree Growth Phenology in Forest Ecosystems, *Curr. For. Rep.*, 11, 12, <https://doi.org/10.1007/s40725-025-00245-9>, 2025.
- Skvareninova, J., Sitko, R., Vido, J., Snopková, Z., and Skvarenina, J.: Phenological response of European beech (*Fagus sylvatica* L.) to climate change in the Western Carpathian climatic-geographical zones, *Front. Plant Sci.*, 15, <https://doi.org/10.3389/fpls.2024.1242695>, 2024.
- 910
- Sohn, J. A., Saha, S., and Bauhus, J.: Potential of forest thinning to mitigate drought stress: A meta-analysis, *For. Ecol. Manag.*, 380, 261–273, <https://doi.org/10.1016/j.foreco.2016.07.046>, 2016.
- Stagakis, S., Markos, N., Vanikiotis, T., Levizou, E., and Kyparissis, A.: Multi-Year Monitoring of Deciduous Forests Ecophysiology and the Role of Temperature and Precipitation as Controlling Factors, *Plants*, 11, 2257, <https://doi.org/10.3390/plants11172257>, 2022.
- 915
- Stitt, M.: Rising CO₂ levels and their potential significance for carbon flow in photosynthetic cells, *Plant Cell Environ.*, 14, 741–762, <https://doi.org/10.1111/j.1365-3040.1991.tb01440.x>, 1991.
- 920
- Sturtevant, C., Ruddell, B. L., Knox, S. H., Verfaillie, J., Matthes, J. H., Oikawa, P. Y., and Baldocchi, D.: Identifying scale-emergent, nonlinear, asynchronous processes of wetland methane exchange, *J. Geophys. Res. Biogeosciences*, 121, 188–204, <https://doi.org/10.1002/2015JG003054>, 2016.



- Tamrakar, R., Rayment, M. B., Moyano, F., Mund, M., and Knohl, A.: Implications of structural diversity for seasonal and annual carbon dioxide fluxes in two temperate deciduous forests, *Agric. For. Meteorol.*, 263, 465–476, <https://doi.org/10.1016/j.agrformet.2018.08.027>, 2018.
- 925 The MathWorks Inc: MATLAB version: 9.12.0 (R2022a), 2022.
- Thomas, F. M., Preusser, S., Backes, B., and Werner, W.: Leaf traits of Central-European beech (*Fagus sylvatica*) and oaks (*Quercus petraea/robur*): Effects of severe drought and long-term dynamics, *For. Ecol. Manag.*, 559, 121823, <https://doi.org/10.1016/j.foreco.2024.121823>, 2024.
- Tian, M., Salmon, Y., Lintunen, A., Oren, R., and Hölttä, T.: Seasonal dynamics and punctuated carbon sink reduction suggest photosynthetic capacity of boreal silver birch is reduced by the accumulation of hexose, *New Phytol.*, 243, 894–908, <https://doi.org/10.1111/nph.19883>, 2024.
- 930
- Torrence, C. and Compo, G. P.: A Practical Guide to Wavelet Analysis, *Bull. Am. Meteorol. Soc.*, 79, 61–78, [https://doi.org/10.1175/1520-0477\(1998\)079%3C0061:APGTWA%3E2.0.CO;2](https://doi.org/10.1175/1520-0477(1998)079%3C0061:APGTWA%3E2.0.CO;2), 1998.
- Trankler, H.-R. and Kanoun, O.: Recent advances in sensor technology, in: IMTC 2001. Proceedings of the 18th IEEE Instrumentation and Measurement Technology Conference. Rediscovering Measurement in the Age of Informatics (Cat. No.01CH 37188), IMTC 2001. Proceedings of the 18th IEEE Instrumentation and Measurement Technology Conference. Rediscovering Measurement in the Age of Informatics (Cat. No.01CH 37188), 309–316 vol.1, <https://doi.org/10.1109/IMTC.2001.928831>, 2001.
- 935
- Vitasse, Y.: Ontogenic changes rather than difference in temperature cause understory trees to leaf out earlier, *New Phytol.*, 198, 149–155, <https://doi.org/10.1111/nph.12130>, 2013.
- 940
- Vitasse, Y. and Basler, D.: What role for photoperiod in the bud burst phenology of European beech, *Eur. J. For. Res.*, 132, 1–8, <https://doi.org/10.1007/s10342-012-0661-2>, 2013.
- Wankmüller, F. J. P., Delval, L., Lehmann, P., Baur, M. J., Cecere, A., Wolf, S., Or, D., Javaux, M., and Carminati, A.: Global influence of soil texture on ecosystem water limitation, *Nature*, 635, 631–638, <https://doi.org/10.1038/s41586-024-08089-2>, 2024.
- 945
- Wu, J., van der Linden, L., Lasslop, G., Carvalhais, N., Pilegaard, K., Beier, C., and Ibrom, A.: Effects of climate variability and functional changes on the interannual variation of the carbon balance in a temperate deciduous forest, *Biogeosciences*, 9, 13–28, <https://doi.org/10.5194/bg-9-13-2012>, 2012.
- Wutzler, T., Lucas-Moffat, A., Migliavacca, M., Knauer, J., Sickel, K., Šigut, L., Menzer, O., and Reichstein, M.: Basic and extensible post-processing of eddy covariance flux data with REddyProc, *Biogeosciences*, 15, 5015–5030, <https://doi.org/10.5194/bg-15-5015-2018>, 2018.
- 950
- Xiao, J., Baldocchi, D., Ichii, K., Li, F., and Papale, D.: Insights into terrestrial carbon and water cycling from the global eddy covariance network, *Nat. Rev. Earth Environ.*, 7, 60–79, <https://doi.org/10.1038/s43017-025-00743-1>, 2026.
- Xie, Q., Moore, C. E., Cleverly, J., Hall, C. C., Ding, Y., Ma, X., Leigh, A., and Huete, A.: Land surface phenology indicators retrieved across diverse ecosystems using a modified threshold algorithm, *Ecol. Indic.*, 147, 110000, <https://doi.org/10.1016/j.ecolind.2023.110000>, 2023.
- 955



Yu, X., Orth, R., Reichstein, M., Bahn, M., Klosterhalfen, A., Knohl, A., Koebsch, F., Migliavacca, M., Mund, M., Nelson, J. A., Stocker, B. D., Walther, S., and Bastos, A.: Contrasting drought legacy effects on gross primary productivity in a mixed versus pure beech forest, *Biogeosciences*, 19, 4315–4329, <https://doi.org/10.5194/bg-19-4315-2022>, 2022.

960 Zahnd, C., Arend, M., Kahmen, A., and Hoch, G.: Microclimatic gradients cause phenological variations within temperate tree canopies in autumn but not in spring, *Agric. For. Meteorol.*, 331, 109340, <https://doi.org/10.1016/j.agrformet.2023.109340>, 2023.

Zani, D., Crowther, T. W., Mo, L., Renner, S. S., and Zohner, C. M.: Increased growing-season productivity drives earlier autumn leaf senescence in temperate trees, *Science*, 370, 1066–1071, <https://doi.org/10.1126/science.abd8911>, 2020.

965 Zohner, C. M., Mirzaghali, L., Renner, S. S., Mo, L., Rebindaine, D., Bucher, R., Palouš, D., Vitasse, Y., Fu, Y. H., Stocker, B. D., and Crowther, T. W.: Effect of climate warming on the timing of autumn leaf senescence reverses after the summer solstice, *Science*, 381, eadf5098, <https://doi.org/10.1126/science.adf5098>, 2023.